A finite volume framework for damage and fracture prediction in wire drawing

Andrew Whelan[1,2,3,5], Vikram Pakrashi[1,2,3,5], Philip Cardiff[1,2,3,4,5*]

[1*]School of Mechanical and Materials Engineering, University College Dublin, Ireland.

[2]SFI MaREI Centre, University College Dublin, Ireland.

[3]UCD Centre for Mechanics, University College Dublin, Ireland.

[4]SFI I-Form Centre, University College Dublin, Ireland.

[5]Bekaert University Technology Centre, University College Dublin, Ireland.

*Corresponding author. E-mail: philip.cardiff@ucd.ie

Abstract

This article presents the implementation of the canonical Lemaitre and Gurson-Tvergaard-Needleman (GTN) damage models and a more recent phase-field type model within a Lagrangian, geometrically nonlinear, cell-centred finite volume framework. The proposed segregated solution procedure uses Picard-type deferred/defect-correction outer corrections, where the primary unknowns are cell-centre displacements and pressures. Spurious zero-energy modes (numerical oscillations in displacement and pressure) are avoided by introducing stabilisation/smoothing diffusion terms in the pressure and momentum equations. Appropriate scaling of the momentum "Rhie-Chow" stabilisation term is shown to be important in regions of plasticity and damage. To accurately predict damage and fracture in wire drawing where hydrostatic pressure is high, novel variants of the Lemaitre model with crack-closure and triaxiality effects and phase field model with non-local effects are proposed. The developed methods are assessed against experimental measurements for three elastoplastic benchmark cases: (i) flat notched bar, (ii) notched round bar, and (iii) axisymmetric wire drawing. The proposed finite volume approach provides a robust basis for predicting damage in wire drawing, where the proposed novel Lemaitre model with crack-closure effects was shown to be the most suitable for predicting experimentally observed fracture in wire drawing.

Keywords: finite volume method, damage, fracture, Lemaitre, Gurson-Tvergaard-Needleman, phase field model, OpenFOAM

1 Introduction

Numerical simulations of ductile fracture problems are of great interest in industries such as aerospace [1, 2], automotive [3–6], nuclear [7], and forming industries [8–13] to allow for the prediction of where and when damage or fracture will occur. The availability of computational predictive tools allows for substantial savings in the cost of experiments and design optimisation.

Its manufacturing process will consist of various combinations of wire-drawing steps, flat rolling, and profiled rollers to achieve the desired profile geometry for a given wire. These processes can often lead to the development of defects and even fracture of the wire during production. By improving understanding of how and why fracture occurs, processes can be optimised to ensure the resulting product is as robust as possible. A computational model for ductile fracture should predict several features, such as the stress and strain distribution, crack/damage origination and propagation and the resulting loss of load-carrying capacity - making coupled damage models of interest for this work.

In the review of Besson [14] the fracture models that have been developed were classified into global and local approaches. The Rice J-integral model is the canonical global approach. This approach suffers from limitations, however, such as that it cannot predict crack initiation and propagation, and the J-integral is also not a material property as it strongly depends on the specimen geometry [15]. These problems were rectified by the J-Q integral approach; however, this approach, in turn, has the limitation that it does not apply to complex geometries [16]. Further developments in this family of models, such as the critical crack tip opening displacement or crack tip opening angle, share the same limitations [17, 18]. These models have been implemented in finite element solvers with remeshing techniques needed to model the crack propagation.

The limitations of the global approach have led to the development of local approaches. In these approaches, a more physically detailed approach is used to characterise the fracture zone. These models can, in turn, be split into surface models (cohesive zone models (CZM)), where fracture occurs on a surface and volume models, where damage or degradation occurs in a volume. The CZM approach is limited because it exhibits strong mesh dependency and often requires a predefined crack path. This thesis will focus on the volume or continuum damage mechanics (CDM) approach and the micro-mechanical approach, which will be described later.

Within the past 15 years, the phase field approach to ductile fracture has gained more attention in the literature [19–23]. This approach involves diffusing the sharp crack over a continuum. Models of this form have been implemented here and will be further described later in this work.

While the models described above have been implemented using the finite element method (FEM), they have not been implemented using the finite volume method (FVM) to the authors' knowledge. The Lagrangian approach is commonly used in metal forming simulations because it more effectively captures effects such as elasticity and residual stress than the Eulerian approach. However, the Lagrangian approach can lead to mesh deterioration, which requires adaptive mesh smoothing and field advection (remapping) at each time step [24, 25]. Unlike conventional finite element methods, the finite volume method (FVM) is well suited for handling these advection problems due to its conservative nature. In addition to the Eulerian and Lagrangian methods, there exist hybrid approaches which have characteristics of each of these approaches, most notably the Arbitrary Lagrangian-Eulerian method [26].

While the finite element method (FEM) is most commonly used in structural applications, more recently there has been an increasing development and use of the finite volume method (FVM) [27]. A wide variety of areas in solid and fluid mechanics have been studied using the finite-volume method such as elastoplasticity [11, 13, 28–32], contact mechanics [29, 33, 34], cohesive zone modelling (CZM) [35, 36], fracture simulation [37] and fluid-solid interactions [38–42]. According to this literature, the strongly conservative properties of the finite volume method make it suitable for such problems.

Both Eulerian and Lagrangian approaches have been used, however, issues have arisen with the Eulerian approach for metal forming problems. There have been challenges with handling the advection of material particles through the domain [24, 25]. By contrast, the Lagrangian approach does not deal with this issue. The updated Lagrangian approach described in [13] is primarily used in this work [1].

For nonlinear problems, the choice between Finite Element and Finite Volume methods remains ambiguous because of several unresolved numerical issues such as unintended hourglass patterns and pressure oscillations, issues of shear and volume locking, reduced convergence rates for strains and stresses compared to displacements, and susceptibility to mesh irregularities [44]. Finite volume discretisations hold the potential to address these challenges in a unique manner [27].

Finite volume methods stand out for their accuracy and absence of excessive stiffness behaviour, a contrast to the locking phenomena commonly seen in fully integrated finite element methods [27]. Notably, a significant advantage of many finite volume methods lies in their order of accuracy. Unlike numerous finite element schemes where the error in strain and stress decreases at a rate that approximates the first order, finite volume methods often exhibit a second-order rate of reduction in these errors, mirroring the pattern observed for displacements [45]. In the current landscape, as computational models grow in size and with the surge in supercomputing and cloud computing capabilities, the emphasis on code parallelization has magnified. Finite volume methods, both fluid and solid types, have been particularly adaptive in this regard. Leveraging iterative linear solvers, tools like OpenFOAM are designed to harness hundreds or even thousands of CPU cores. This contrasts with many finite element strategies, which historically have favoured direct linear solvers. Consequently, their parallel efficiency tends to be restricted relative to iterative solvers, making the deployment on vast numbers of CPU cores less prevalent [27].

The cell-centred finite volume method is used in this work where the unknowns are specified at the centre of the control volumes. Demirdžić et al. [46] first proposed using the cell-centred finite volume method in its modern form for solid mechanics 30 years ago. This method was further developed by Demirdžić and Muzaferija [47] who generalised the original 2-D method to 3-D convex polyhedral cells. Another class of cell-centred method are the explicit Godunov-type cell-centred approaches based on the work of Trangenstein and Colella [48]. This method was initially used to model the 1-D propagation of waves in elasto-plastic solids but has since been extended in

[1] More specifically this is the incrementally updated Lagrangian method [43]

various forms to 3-D grids [49–54]. These methods, as well as other finite-volume based methods, are described in more detail in Cardiff and Demirdžić [27].

ADD Explicit contribution/novelties of this paper. There are three main things: FVM approach, layer addition/removal, and novel forms of damage model. These models are implemented in OpenFOAM, an open-source C++ software that uses the finite volume method to solve solid and fluid mechanics problems. In particular, they have been implemented in the solids4foam OpenFOAM toolbox [**?** **?**], building on previous work [13, 55].

The remainder of the paper is organised as follows: Section 2 describes the details of the mathematical model, including the governing momentum equation in Lagrangian form and the elastoplastic damage laws. Section **??** presents the proposed geometrically nonlinear, cell-centred finite volume framework, including stabilisation terms and the segregated solution algorithm details. The accuracy and robustness of the proposed numerical procedures are assessed against three experimental benchmark cases in Section 4 The article ends with a summary of the main conclusions.

2 Mathematical Model

This section outlines the Lagrangian finite strain finite volume methodology, where details of the constitutive laws are left to Secton 3.

2.1 Linear momentum conservation

The dynamic, Lagrangian, strong integral form of linear momentum conservation for a body Ω, bounded by a surface Γ with outwards pointing normal $\mathbf{n}$, can be equivalently expressed in *total* Lagrangian form as

$$\int_{\Omega_o} \rho_o \frac{\partial^2 \mathbf{u}}{\partial t^2} d\Omega_o = \oint_{\Gamma_o} \left(J\mathbf{F}^{-T} \cdot \mathbf{n}_o \right) \cdot \boldsymbol{\sigma} \; d\Gamma_o \tag{1}$$

or *updated* Lagrangian form as

$$\int_{\Omega_\mathrm{u}} \frac{\partial}{\partial t} \left(\rho_u \frac{\partial \mathbf{u}}{\partial t} \right) d\Omega_u = \oint_{\Gamma_\mathrm{u}} \left(j\mathbf{f}^{-T} \cdot \mathbf{n}_u \right) \cdot \boldsymbol{\sigma} \; d\Gamma_\mathrm{u} \tag{2}$$

where ρ is the density, $\mathbf{u}$ is the displacement vector, $\boldsymbol{\sigma}$ is the true (Cauchy) stress, and body forces are neglected. Subscript o indicates quantities in the initial reference configuration, and subscript u indicates quantities in the updated configuration. The two forms are connected through Nanson's formula [56], which relate the deformed area vector $\mathbf{\Gamma}$ with the initial area vector $\mathbf{\Gamma}_o$:

$$\mathbf{\Gamma} = J\mathbf{F}^{-T} \cdot \mathbf{\Gamma}_o \tag{3}$$

where the deformation gradient is defined as $\mathbf{F} = \mathbf{I} + (\boldsymbol{\nabla} \boldsymbol{u})^T$ and its determinant (Jacobian) as $J = \det(\boldsymbol{F})$. The *relative* deformation gradient is given in terms of the displacement increment as $\mathbf{f} = \mathbf{I} + \nabla(\Delta\mathbf{u})^T$ and the relative Jacobian as $j = \det(\mathbf{f})$.

Although the total Lagrangian approach is a viable option, the current work adopts the updated Lagrangian approach as developing Eulerian-type upstream and downstream mesh layer addition and removal conditions is conceptually easier in an updated Lagrangian formulation, as described in Section 2.4.

The definition of the true stress in Equations 1 and 2 comes from the constitutive law, as is described in Section 3.

2.2 Solution Domain Discretisation

The solution domain is discretised in space and time. The total specified simulation time is divided into a finite number of time increments Δt, and the discretised governing momentum equation is solved in a time-marching manner.

The space domain is divided into a finite number of contiguous convex polyhedral cells. The proposed solution discretisation follows closely the approach of Cardiff et al. [13]; consequently, only an overview of the final discretised form of equations and adopted solution algorithm are given below.

To facilitate the use of a segregated solution algorithm, the surface forces term (term on the right-hand side of Equation 2) is split into explicit and implicit components:

$$\begin{aligned}\int_{\Omega_\mathrm{u}} \frac{\partial}{\partial t}\left(\rho_u \frac{\partial \mathbf{u}}{\partial t}\right) d\Omega_u = &\underbrace{\oint_{\Gamma_u} K_{imp}\ \mathbf{n}_u \cdot \nabla\left(\Delta \mathbf{u}\right)\, d\Gamma_u}_{\text{implicit}} \\ &+ \underbrace{\oint_{\Gamma_\mathrm{u}} (j\mathbf{f}^{-T} \cdot \mathbf{n}_u) \cdot \boldsymbol{\sigma}\, d\Gamma_\mathrm{u} - \oint_{\Gamma_u} K_{imp}\ \mathbf{n}_u \cdot \nabla\left(\Delta \mathbf{u}\right)\, d\Gamma_u}_{\text{explicit}} \end{aligned} \tag{4}$$

where the first term on the right-hand side (Laplacian term) is treated implicitly, and the second and third terms on the right-hand side are treated explicitly. Here, by implicit, we mean that the term contributes coefficients to the resulting linear(-ised) system of equations, while the explicit terms will contribute only to the source of the system of linear equations. The overall procedure will be implicit in time in that the time step size is not constrained by the Courant–Friedrichs–Lewy condition. This Laplacian term can be considered an approximate compact-stencil linearisation of the surface stress term. This allows the coupled vector system to be temporarily decoupled in three scalar component equations. This allows the scalar component equations to be solved independently, where outer Picard iterations provide the inter-component coupling. Unlike Newton-Raphson approaches, where quadratic convergence may be expected, we can expect linear convergence of the residuals when using a segregated approach; however, this disadvantage is offset in several ways: (i) an exact Jacobian stiffness matrix need not be assembled, which is often costly; (ii) a material tangent is not required for the material laws, as instead the scalar coefficient K_{imp} is only required; (iii) outer Picard iterations are less expensive than Newton iterations as the discretised systems are smaller to assemble and quicker to solve; (iv) Picard iteration may provide superior convergence when the solution is far from the asymptotic region, potentially resulting in a more robust approach for highly nonlinear large strain fracture and damage cases. Nonetheless, as noted previously [29], segregated solution procedures can suffer slow convergence relative to coupled approaches, particularly in high aspect ratio linear cases. In the current work, K_{imp} is chosen following the work of Jasak and Weller [57] as

$$K_{imp} = \frac{4}{3}\mu + \kappa \tag{5}$$

where μ is the material shear modulus and κ is the bulk modulus. It should be reinforced that the value of K_{imp} affects convergence but does not affect the final converged solution, assuming convergence is achieved.

The primary unknown to be solved for is the displacement increment $\Delta \boldsymbol{u} = \boldsymbol{u}^{[m+1]} - \boldsymbol{u}^{[m]}$ where the $[m]$ superscript indicates a quantity from the previous time-step and $[m+1]$ a quantity from the current (to be calculated) time step.

The resulting conservation equation (Equation 4) is applied to each cell (control volume) in the computational mesh and discretised in terms of the displacement increment at the cell centre/centroid $(\Delta \mathbf{u})_P$ and at the centres of the neighbouring cells N_i.

The temporal volume integral term is discretised in space using the mid-point rule and discretised in time using a first-order accurate implicit backward Euler scheme [57]:

$$\begin{aligned}
\int_{\Omega_u} \frac{\partial}{\partial t}\left(\rho_u \frac{\partial(\Delta \mathbf{u})}{\partial t}\right) d\Omega_u &\approx \frac{\partial}{\partial t}\left(\rho_u \frac{\partial(\Delta \mathbf{u})}{\partial t}\right)_P \Omega_P \\
&\approx \left(\frac{\rho_u^{[m+1]} \frac{\partial(\Delta \mathbf{u})}{\partial t}^{[m+1]} - \rho_u^{[m]} \frac{\partial(\Delta \mathbf{u})}{\partial t}^{[m]}}{\Delta t}\right)_P \Omega_P \\
&\approx \left[\frac{\rho_u^{[m+1]}\left(\frac{\Delta \mathbf{u}^{[m+1]} - \Delta \mathbf{u}^{[m]}}{\Delta t}\right) - \rho_u^{[m]}\left(\frac{\Delta \mathbf{u}^{[m]} - \Delta \mathbf{u}^{[m-1]}}{\Delta t}\right)}{\Delta t}\right]_P \Omega_P \\
&\approx \frac{1}{\Delta t^2}\left[\rho_{u_P}^{[m+1]} \Delta \mathbf{u}_P^{[m+1]} - \left(\rho_{u_P}^{[m+1]} + \rho_{u_P}^{[m]}\right) \Delta \mathbf{u}_P^{[m]} + \rho_{u_P}^{[m]} \Delta \mathbf{u}_P^{[m-1]}\right] \Omega_P
\end{aligned} \tag{6}$$

The $\boldsymbol{u}^{[m-1]}$ term is discretised in a similar fashion, noting that $\boldsymbol{u}^{[m]} = \boldsymbol{u}^{[m-1]} + \Delta \boldsymbol{u}$ in Equation 4.

The surface forces Laplacian term (first term on the right-hand side of Equation 4) is discretised using central differencing with over-relaxed non-orthogonal correction [13, 28, 34, 57, 58]:

$$\begin{aligned}
\oint_{\Gamma_u} K_{imp} \mathbf{n}_u \cdot \nabla (\Delta \mathbf{u})\, d\Gamma_u \approx & \sum_{f \in N_f} K_{imp}^f \left|\boldsymbol{\Delta}_{u_f}\right| \left(\frac{\Delta \mathbf{u}_{N_f} - \Delta \mathbf{u}_P}{|\mathbf{d}_f|}\right) \left|\boldsymbol{\Gamma}_{u_f}\right| \\
& + \sum_{f \in N_f} K_{imp}^f\, \mathbf{k}_{u_f} \cdot \left[\boldsymbol{\nabla} (\Delta \mathbf{u})\right]_f \left|\boldsymbol{\Gamma}_{u_f}\right|
\end{aligned} \tag{7}$$

where N_f represents the set of faces f in cell P, where neighbouring cell centre N_f shares face f with the cell P. The over-relaxed orthogonal vector $\boldsymbol{\Delta}_{u_f} = \frac{\boldsymbol{d}_{u_f}}{\boldsymbol{d}_{u_f} \cdot \boldsymbol{n}_{u_f}}$ and non-orthogonal correction vector is $\boldsymbol{k}_{u_f} = \boldsymbol{n}_{u_f} - \boldsymbol{\Delta}_{u_f}$, where $\boldsymbol{n}_{u_f}$ is the outward-facing unit normal to the face f. The first term on the right-hand side is treated implicitly, while the second term - representing non-orthogonal corrections at the face - is treated explicitly.

The remaining surface force terms (second and third terms on the right-hand side of Equation 4) are discretised by assuming that they vary linearly across the face as follows [59]:

$$\oint_{\Gamma_{\mathrm{u}}} (j\mathbf{f}^{-T} \cdot \mathbf{n}_u) \cdot \boldsymbol{\sigma} \; d\Gamma_{\mathrm{u}} \approx \sum_{f \in N_f} \boldsymbol{\Gamma}_{u_f} \cdot \left(j\boldsymbol{\sigma} \cdot \mathbf{f}^{-T} \right)_f \tag{8}$$

$$\oint_{\Gamma_u} K_{imp} \; \mathbf{n}_u \cdot \boldsymbol{\nabla} \left(\Delta \mathbf{u} \right) \, d\Gamma_u \approx \sum_{f \in N_f} K_{imp} \; \boldsymbol{\Gamma}_{u_f} \cdot \left[\boldsymbol{\nabla} \left(\Delta \mathbf{u} \right) \right]_f \tag{9}$$

The terms at a face, indicated by the subscript f, are calculated by linearly interpolating from the adjacent cell-centre values. The cell-centre gradients $\boldsymbol{\nabla}\left(\Delta\mathbf{u}\right)$ are determined using a least squares method [59].

All dependent variables must be specified at the initial time. Boundary conditions must be applied to the faces that coincide with the boundary of the solution domain. The discretised expressions on boundary faces are modified to account for either the known displacement components in Dirichlet conditions or the known traction for Neumann conditions. Coulomb friction contact boundaries are handled using an iterative penalty method, as described previously [13, 33]. More recent segment-to-segment finite volume contact procedures could also be used [60, 61].

2.2.1 Rhie-Chow Stabilisation

The difference in the computational stencil for the first and third terms on the right-hand side in Equation 4 introduces third-order numerical diffusion to the discretisation, which quells spurious zero-energy checkerboarding solution oscillations. First introduced by Rhie and Chow [62] for cell-centred finite volume methods, This approach was first proposed for cell-centred solid mechanics procedures by Demirdžić and Muzaferija [63], based on the earlier approach of Rhie and Chow Demirdžić and Muzaferija [63]. In the current approach, the so-called Rhie-Chow stabilisation term $\mathcal{D}_{\text{Rhie-Chow}}$ takes the following form:

$$\mathcal{D}_{\text{Rhie-Chow}} = \sum_{f \in N_f} K^f_{imp} \left[|\boldsymbol{\Delta}_f| \, \frac{\Delta \boldsymbol{u}_{N_f} - \Delta \boldsymbol{u}_P}{|\boldsymbol{d}_f|} - \boldsymbol{\Delta}_f \cdot (\boldsymbol{\nabla}(\Delta \boldsymbol{u}))_f \right] \tag{10}$$

which comes from the difference between Equations 7 and 9. The first term on the right-hand side represents a compact stencil (two-node) approximation of the face normal gradient, while the second term represents a larger stencil approximation. In the limit of mesh refinement, these two terms cancel out; otherwise, they produce a stabilisation effect which tends to smooth the solution fields. As the term reduces at a third-order rate, it does not affect the overall scheme's second-order accuracy.

As shown in Section 4, the magnitude of the Rhie-Chow stabilisation affects the localisation behaviour for damage and fracture mechanics models, with a tendency to artificially *smear out* damage fields. Two mitigation strategies are proposed here to produce a modified Rhie-Chow stabilisation $\hat{\mathcal{D}}_{\text{Rhie-Chow}}$:

- The Rhie-Chow stabilisation is scaled by a global scalar constant $0 \leq \mathcal{R}$ supplied by the user:

$$\hat{\mathcal{D}}_{\text{Rhie-Chow}} = \mathcal{R}\ \mathcal{D}_{\text{Rhie-Chow}} \tag{11}$$

- The Rhie-Chow stabilisation is scaled by a global scalar constant in addition to a damage-dependent field:

$$\hat{\mathcal{D}}_{\text{Rhie-Chow}} = \mathcal{R}(1-D)^2\ \mathcal{D}_{\text{Rhie-Chow}} \tag{12}$$

In the first approach, the smoothing effect is reduced globally with the result that the smearing of damage fields is reduced; however, the disadvantage of this approach is that solution convergence is slowed as the stabilisation term is reduced in magnitude; in addition, numerical oscillations are more likely to appear, particularly in regions undergoing purely elastic deformation where no dissipation mechanisms exist. In the second approach, a damage variable $0 < D \leq 1$ (to be introduced in Section 3) reduces the smoothing effect only in regions of damage. The effect of these proposed modifications are examined in Section 4.

2.2.2 Hydrostatic Pressure Calculation

As is well-known, displacement-only formulations are susceptible to displaying numerical hydrostatic pressure oscillations in regions of large isochoric plastic strains. In Cardiff et al. [13], it was proposed to smooth the relative deformation gradient Jacobian field. In contrast, the current approach forms and solves a pressure Poisson equation:

$$p = -\frac{\kappa}{2}(J^2 - 1) + \mathcal{D}^p_{\text{Rhie-Chow}} \tag{13}$$

where $p = -\text{tr}(\boldsymbol{\sigma})/3$ is the hydrostatic pressure and trace operator is indicated by $\text{tr}(\bullet)$. The Rhie-Chow pressure stabilisation term $\mathcal{D}^p_{\text{Rhie-Chow}}$ is discretised according to Equation 10 with the displacement increment $\Delta \boldsymbol{u}$ replaced by the pressure p. As in the case of the discretised momentum equation, the magnitude of the Rhie-Chow stabilisation term can be controlled with a global scale constant $0 \leq \mathcal{R}_p$ supplied by the user. The effect of the Rhie-Chow stabilisation term here is to smooth out any pressure oscillations. The final form stabilised form of the pressure Poisson equation is

$$p - \mathbb{D}\boldsymbol{\nabla}^2 p = -\frac{\kappa}{2}(J^2 - 1) - \boldsymbol{\nabla} \cdot (\mathbb{D}\boldsymbol{\nabla} p) \tag{14}$$

where the terms on the left-hand side are discretised implicitly and the terms on the right-hand side are discretised explicitly, following similar methods to Equations 6 and 7. The second terms on the left and right-hand sides come from the Rhie-Chow stabilisation. The described approach is similar to the formulation proposed by Bijelonja et al. [64–67] for incompressibility, quasi-incompressibility and elastoplasticity.

2.3 Solution Algorithm

The linear momentum equation is discretised for each control volume P, and a linear algebraic equation of the following form is assembled [57].

$$a_p \Delta \mathbf{u}_p + \sum_F a_n \Delta \mathbf{u}_n = \mathbf{b}_p \tag{15}$$

Where a_p is the central coefficient, a_n are the coefficients associated with the centre of neighbouring cells, F is the number of internal faces of the control volume, $\mathbf{b}_p$ is the source vector contribution.

These linear algebraic equations are then assembled for all control volumes creating a system of linear algebraic equations:

$$\mathbf{K}\mathbf{u} = \mathbf{f} \tag{16}$$

Where $\mathbf{K}$ is an $M \times M$ coefficient matrix containing the implicit operators where M is the total number of control volumes. The solution vector $\mathbf{u}$ contains the unknown cell-centre displacement increments $\Delta\mathbf{u}$. $\mathbf{f}$ is the source term containing the explicit operators. A similar scalar system is formed and solved for the hydrostatic pressure (Equation 14) during the calculation of the stress.

As noted in Section 2.2, a segregated solution algorithm is employed where the governing vector momentum equation is temporarily decoupled and three scalar equations are solved; outer Picard iterations at each time stpe provide the inter-equation coupling.

The *inner* linear sparse system is iteratively solved using an incomplete Cholesky preconditioned conjugate gradient method [68]. As noted in previous articles on segregated methods, the inner system need not be solved to a tight tolerance as coefficients and source terms are approximated from the previous increment; a reduction in the residuals of one order of magnitude is typically sufficient. The outer iterations are performed until the predefined tolerance, typically 1×10^{-6}, has been achieved [13].

In the current updated Lagrangian approach, the mesh is moved to the deformed configuration at the end of each time step. Given that the displacements are calculated at the cell centres, interpolation must be performed to calculate the displacements at the vertices to update the mesh. A linear least-squared method is employed here [13].

The procedures have been implemented and publicly shared within the solids4foam toolbox [**?** **?**] of the open-source OpenFOAM software.

An overview of the solution algorithm is shown in Algorithm 1.

Algorithm 1: Solution Procedure

for all time steps **do**
  while convergence not reached **do**
  - Discrete governing system (Equation 4) for each cell, using Equations 5-10, in terms of $\Delta\mathbf{u}$
  - Assemble the discretised equations for all cells into three scalar linear systems (Equation 14)
  - Solve the three scalar linear systems in terms of cell-centred displacement increments $\Delta\mathbf{u}$
  - Update/reconstruct the kinematics: $\boldsymbol{\nabla}(\boldsymbol{\Delta u})$, $\boldsymbol{F}$, J, $\boldsymbol{f}$, j
  - Update the stress ($\boldsymbol{\sigma}$) at the cell-centres using the chosen material law
  - Update the Rhie-Chow stabilisation: $\hat{\mathcal{D}}_{\text{Rhie-Chow}}$
  end while - Interpolate cell-centre displacement increments to the vertices
  - Move mesh to the deformed configuration using the vertex displacements, incorporating layer addition/removal (Section 2.4)
end for

2.4 Eulerian-Type Layer Addition and Removal Boundaries

Steady-state behaviour is typically the primary interest in wire drawing and other continuous forming approaches. Eulerian approaches are a natural choice but are not commonly employed when elastic phenomena (e.g. spring back, residual stresses) are important. When simulating wire drawing using a Lagrangian approach, a naïve approach is to simulate a workpiece segment that is *long enough* to allow steady-state to be reached. The disadvantage of this approach is that computational cost is inflated by the portion of the workpiece domain primarily undergoing rigid-body translation, which may be large relative to the region undergoing plastic deformations.

To overcome this disadvantage, the current work proposes Eulerian-type layer addition and removal conditions for the workpiece upstream and downstream boundaries. The approach involves fixing the workpiece (e.g., wire) upstream and downstream mesh boundaries in space during the mesh motion at the end of each time step. As cells near the upstream boundary become elongated, layers of new cells are added. Similarly, cells are removed as they become compressed near the downstream patch. In this way, the length of the workpiece domain remains fixed (like an Eulerian approach), but a traditional Lagrangian method is still used to calculate the deformation.

Figure 1 schematically outlines the step involved in the layer addition and removal mesh motion scheme:

(a) The workpiece (e.g., wire) mesh is constructed such that it is layered in the streamwise direction;
(b) Solution of the discretised governing equations provides the cell centres displacement increments $\Delta\boldsymbol{u}$;
(c) The cell-centred displacement increment $\Delta\boldsymbol{u}$ are interpolated to the vertices $\Delta\boldsymbol{u}_v$;
(d) If the average width (in the streamwise direction) of the cell layer d_{av} is greater at the upsrteam boundary than a user-prescribed maximum width d_{max}, a zero-thickness layer of cells at the upstream boundary. The displacement increments of the newly added layer of vertices are taken from the upstream boundary vertices;
(e) The vertex displacement increments $\Delta\boldsymbol{u}_v$ at the upstream and downstream boundaries are set to zero, except for the newly added vertices part of the zero-thickness layer;
(f) The mesh is moved by the vertex displacement increment field $\Delta\boldsymbol{u}_v$, where it is noted that the vertices on the upstream and downstream points do not move;

(g) If the average width (in the streamwise direction) of the cell layer d_{av} at the downstream boundary is less than a user-prescribed minimum width d_{min}, remove the layer of cells at the downstream boundary. Depending on displacement increment magnitude, multiple cell layers may need to be removed.

Fig. 1 Layer addition and removal mesh motion algorithm

Following the layer addition and removal mesh motion algorithm, solution and derived field data at the newly added cell centres are mapped from the field data stored at the upstream boundary. This mapping approach assumes field data to have a zero gradient in the upstream direction; this assumption is valid if the upstream and downstream are chosen sufficiently far from the *active* deformation zone.

Note on parallelisation: The proposed solution algorithm has been implemented in the open-source toolbox OpenFOAM, where multi-CPU-core parallelisation on distributed memory systems is achieved through the domain decomposition approach. To simplify the implementation of the non-trivial topological mesh changes (addition or removal of cells), domain decomposition approaches have been limited to decomposing the workpiece into streamwise columns of cells (Figure 2). In the current approach, modified forms of the METIS [69] and scotch [70] approaches have been used to perform this decomposition.

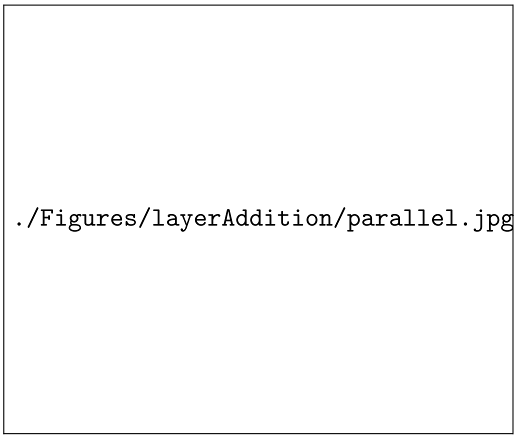

Fig. 2 Example parallel decomposition of a wire and drawing die, where the wire is decomposed into streamwise *columns*, indicated by the different colours. There is no limitation on the die decomposition.

3 Constitutive damage laws

3.1 Overview

As noted by Garrison and Moody [71], ductile fracture in metals occurs in three stages: (i) voids are nucleated at material defects (usually inclusions), adding to pre-existing voids, if any; (ii) plastic deformations cause these voids to grow; and (iii) when large enough, these voids coalesce to form micro-cracks and macro-cracks. Recent reviews of Approaches to model ductile fracture in metal forming can classified into two approaches [9, 10]: continuum damage mechanics models and micro-mechanical models.

In *continuum* damage mechanics, an internal damage variable is used to describe the accumulation of microstructural degradation within a material due to various types of loading. This degradation is typically reflected in the increased density of internal defects, such as microcracks, dislocations, or voids. The internal damage variable is continuous, meaning it can take on any value within a given range. The *micro-mechanical* approach is also continuous in nature and posits the existence of material micro-voids. The void density is described by a variable denoted as porosity. Material degradation is characterised by increased porosity due to void nucleation, growth, and coalescence. As noted by Cao [9], Besson [14] and Tekkaya et al. [10], the canonical frameworks in the continuum damage mechanics and micro-mechanical approaches are the Lemaitre [72, 73] and the Gurson-Tvergaard-Needleman (GTN) [74, 75] models, respectively.

This section provides an overview of the classic Lemaitre and GTN models and proposes modifications to the Lemaitre model to extend its applicability to high hydrostatic pressure regimes characteristic of wire drawing. For comparison, a recent phase field model damage approach is also considered.

The constitutive damage laws described in this section close the system of governing equations (Equation 4) described in Section 2.2, by providing the definition of stress.

3.2 Preliminaries

Before describing these models in more detail, it is necessary to define the stress triaxiality η and the Lode angle θ and related Lode parameters [76, 77]. Extensive literature has noted the importance of stress triaxiality and Lode angle in predicting ductile fracture [9, 10, 14]. The triaxiality parameter η is given by:

$$\eta = -\frac{p}{\sigma_v} \tag{17}$$

where, as noted previously, $p = -\mathrm{tr}(\boldsymbol{\sigma})/3$ is the hydrostatic pressure, and $\sigma_v = \sqrt{3J_2} = \sqrt{\frac{3}{2}\mathrm{dev}(\boldsymbol{\sigma}) : \mathrm{dev}(\boldsymbol{\sigma})}$ is the equivalent (von Mises) stress. J_2 is the second invariant of the deviatoric stress tensor. The deviatoric operator is indicated by $\mathrm{dev}(\bullet)$, and : indicates the double-dot product.

The Lode angle $0 \leq \theta \leq \frac{\pi}{3}$ physical interpretation relates to the degree of shear dominance present in the stress state. It can be rewritten as a function of the normalised third invariant of the deviatoric stress tensor:

$$\theta = \frac{1}{3} \arccos(\xi) \tag{18}$$

The parameter $0 \leq \xi \leq 1$ is determined as a ratio between the third invariant and the equivalent stress:

$$\xi = \left(\frac{r}{\sigma_v}\right)^3 \tag{19}$$

where r is given by:

$$r = 3\left(\frac{3}{2}J_3\right)^{1/3} \tag{20}$$

The third invariant of the deviatoric stress tensor is $J_3 = \det[\mathrm{dev}(\mathbf{s})]$. An alternative normalised Lode angle has been proposed by Bai and Wierzbicki [76] to be

$$\bar{\theta} = 1 - \frac{6\theta}{\pi} \tag{21}$$

which ranges between -1 and 1.

The three Lode parameters (θ, ξ, and $\bar{\theta}$) are essentially equivalent but are defined to vary between different limits.

3.3 Isotropic Elastoplasticity

3.3.1 Model Formulation

In the current work, the damage models are formulated in terms of isotropic J_2 (von Mises) elastoplasticity. Extension to other forms of elastoplasticity (e.g., kinematic hardening, anisotropic/Hill yielding, distortional hardening) is possible but is outside the scope of this article. The adopted large strain elastoplasticity formulation is based on the logarithmic (Hencky) strain, as proposed by Eterovic and Bathe [78] and described in detail by Koji and Bathe [79] and de Souza Neto et al. [80]. This approach allows an additive split of the elastic and plastic strain tensors, conveniently leading to a return mapping scheme that is similar in form to those used in small-strain deformation models. In contrast, previous large-strain elastoplastic models [11, 13] implemented in the OpenFOAM software have adopted the approaches of Caminero et al. [84] and Simo and Hughes [81].

The employed isotropic J_2 elastoplastic constitutive law is defined in terms of the yield criterion

$$\Phi = \sigma_v - \sigma_y(\bar{\varepsilon}_p) \tag{22}$$

and flow rule

$$\dot{\mathbf{F}}_p \cdot \mathbf{F}_p^{-1} = \dot{\bar{\varepsilon}}_p \, \mathbf{R}_e^T \cdot \left[\frac{3}{2} \frac{\operatorname{dev}(\boldsymbol{\sigma})}{\sigma_v} \right] \cdot \mathbf{R}_e \tag{23}$$

where the yield stress σ_y is a function of the hardening variable $\bar{\varepsilon}_p$ coincides with the equivalent plastic strain $\bar{\varepsilon}_p$. The deformation gradient is decomposed into elastic and plastic components $\boldsymbol{F} = \boldsymbol{F}_e \cdot \boldsymbol{F}_p$ and polar decomposition of the elastic deformation gradient gives the elastic rotation $\boldsymbol{R}_e$ and elastic stretch $\boldsymbol{U}_e$ tensors: $\boldsymbol{F}_e = \boldsymbol{R}_e \cdot \boldsymbol{U}_p$.

The model is closed with the Kuhn-Tucker conditions

$$\Phi \geq 0, \qquad \dot{\bar{\varepsilon}}_p \geq 0, \qquad \dot{\bar{\varepsilon}}_p \Phi = 0 \tag{24}$$

and the consistency condition

$$\dot{\bar{\varepsilon}}_p \dot{\Phi} = 0 \tag{25}$$

3.3.2 Computational procedure

For each cell at every outer (Picard) iteration, the stress $\boldsymbol{\sigma}^{[m+1]}$ and history variables ($\alpha^{[m+1]}$, $\boldsymbol{F}_p^{[m+1]}$) at time step $t^{[m+1]}$ must be calculated in terms of the current displacement increment gradient $[\boldsymbol{\nabla}(\Delta \boldsymbol{u})]^{[m+1]}$ and old-time history variables ($\alpha^{[m]}$, $\boldsymbol{F}_p^{[m]}$).

The adopted stress calculation algorithm [80] is summarised in Algorithm 2.

Andrew: why is J not equal to det(F) in pressure calculation?

3.4 Lemaitre damage model

3.4.1 Model Formulation

The Lemaitre model describes damage using a scalar field variable D. When no damage has occurred, the damage variable D equals 0 (virgin material), whereas when the material is fully

Algorithm 2: Large strain J_2 (von Mises) isotropic elastoplastic stress calculation algorithm [80]

(i) Update deformation gradients for a given incremental displacement

$$\mathbf{f}^{[m+1]} = \mathbf{I} + [\boldsymbol{\nabla}(\Delta\mathbf{u})]^T$$

$$\mathbf{F}^{[m+1]} = \mathbf{f}^{[m+1]} \cdot \mathbf{F}^{[m]}$$

(ii) Compute trial elastic state

$$\mathbf{B}_e^{[m]} = \exp\left(2\boldsymbol{\varepsilon}_e^{[m]}\right)$$

$$\mathbf{B}_e^{\text{trial}} = \mathbf{f}^{[m+1]} \cdot \mathbf{B}_e^{[m]} \cdot (\mathbf{f}^{[m+1]})^T$$

$$\boldsymbol{\varepsilon}_e^{\text{trial}} = \frac{1}{2}\ln(\mathbf{B}_e^{\text{trial}})$$

$$\bar{\varepsilon}_p^{\text{trial}} = \bar{\varepsilon}_p^{[m]}$$

$$\sigma_v^{\text{trial}} = \sqrt{3/2}||2G\ \text{dev}(\boldsymbol{\varepsilon}_e^{\text{trial}})||$$

$$\Phi^{\text{trial}} = \sigma_v^{\text{trial}} - \sigma_y(\bar{\varepsilon}_p^{\text{trial}})$$

if $\Phi^{trial} > 0$ **then**
| go to step (iii) to solve for $\Delta\bar{\varepsilon}_p$
else
| $\Delta\bar{\varepsilon}_p = 0$ and go to step (iv)
end

(iii) Use the Newton-Raphson method to solve the yield function for $\Delta\bar{\varepsilon}_p$:

$$\sigma_v^{\text{trial}} - 3\mu\Delta\bar{\varepsilon}_p - \sigma_y(\bar{\varepsilon}_p^{[m]} + \Delta\bar{\varepsilon}_p) = 0$$

(iv) Update constitutive variables and deviatoric stress

$$\boldsymbol{\varepsilon}_e^{[m+1]} = \boldsymbol{\varepsilon}_e^{\text{trial}} - \sqrt{3/2}\ \Delta\bar{\varepsilon}_p \frac{\text{dev}(\boldsymbol{\varepsilon}_e^{\text{trial}})}{||\boldsymbol{\varepsilon}_e^{\text{trial}}||}$$

$$\bar{\varepsilon}_p^{[m+1]} = \bar{\varepsilon}_p^{[m]} + \Delta\bar{\varepsilon}_p$$

$$\boldsymbol{s}^{[m+1]} = (1/J)2\mu\ \text{dev}\left(\boldsymbol{\varepsilon}_e^{[m+1]}\right)$$

(v) Implicitly solve the pressure Poisson's equation, where $J^{[m+1]} = -\kappa\ \text{tr}\left(\boldsymbol{\varepsilon}_e^{[m+1]}\right)$.

$$p^{[m+1]} - \mathbb{D}\boldsymbol{\nabla}^2 p^{[m+1]} = -\frac{\kappa}{2}\left[\left(J^{[m+1]}\right)^2 - 1\right] - \boldsymbol{\nabla}\cdot\left(\mathbb{D}\boldsymbol{\nabla}p_{[i]}^{[m+1]}\right) \tag{26}$$

(vi) Update the true (Cauchy) stress

$$\boldsymbol{\sigma}^{[m+1]} = \boldsymbol{s}^{[m+1]} - p^{[m+1]}\mathbf{I}$$

damaged, the damage variable equals 1. From a physical point of view, D can be interpreted as the area of cracks and cavities per unit surface cut by an arbitrary plane.

The Lemaitre model augments the elastoplasticity constitutive law (Equations 22 and 23) with the inclusion of a damage variable D evolution law, and scaling of the yield function and flow rules by the reciprocal of $(1 - D)$:

$$\Phi = \frac{\sigma_v}{1-D} - \sigma_y(\bar{\varepsilon}_p) \tag{27}$$

$$\dot{\mathbf{F}}_p \cdot \mathbf{F}_p^{-1} = \frac{\dot{\bar{\varepsilon}}_p}{1-D} \mathbf{R}_e^T \cdot \left[\frac{3}{2}\frac{\operatorname{dev}(\boldsymbol{\sigma})}{\sigma_v}\right] \cdot \mathbf{R}_e \tag{28}$$

$$\dot{D} = \frac{\dot{\bar{\varepsilon}}_p}{1-D}\left(\frac{-Y}{S_0}\right)^b \tag{29}$$

where S_0 (dimensions of stress) and b (dimensionless) are material parameters. The energy release rate Y, which gives the energy dissipated due to the phenomenon of damage, is given by [73]

$$Y = -\frac{\sigma_v^2}{2E}\left[\frac{2}{3}(1+\nu) + 3(1-2\nu)\eta^2\right] \tag{30}$$

where E is Young's modulus and ν is Poisson's ratio, where the dependence on triaxiality ($\eta = {}^{p}/_{\sigma_v}$) is explicitly clear.

Triaxiality and Lode Angle Dependence

The classic Lemaitre model does not distinguish between positive and negative triaxiality (η is squared in Equation 30); consequently, it can overpredict damage in wire drawing processes where triaxiality can be highly negative. A simple remedy is to employ a triaxiality cut-off [86], which disallows damage evolution for highly negative triaxiality values:

$$\dot{D} = \begin{cases} 0 & \text{if } \eta \leq -\frac{1}{3} \\ \frac{\dot{\bar{\varepsilon}}_p}{1-D}\left(\frac{-Y}{S_0}\right)^b & \text{if } \eta > -\frac{1}{3} \end{cases} \tag{31}$$

Rather than use a triaxiality cut-off, Malcher and co-workers [91–93] proposed that the parameter S_0 be a function of triaxiality η as well as Lode angle ξ. This approach has shown an ability to accurately predict fracture for a range of loading conditions, at both low and high triaxiality values and for various shear stress states. The Malcher et al. form of damage evolution is achieved by making S_0 in Equation 29 a function of η and ξ:

$$S(\eta, \xi) = \frac{S_{0.33}}{3|\eta| + \frac{S_{0.33}}{S_{0.0}}(1-\xi^2)} \tag{32}$$

where $S_{0.33}$ and $S_{0.0}$ are material parameters, which were determined based on pure tensile loading $S_{0.33}$ and pure shear loading ($S_{0.0}$).

Despite its success, one weakness of this formulation is that it does not distinguish between positive and negative triaxiality values, which is critical for wire drawing. To overcome this limitation, a function for $S(\eta, \xi)$ is proposed here, inspired by the Ko criterion [132] uncoupled damage law. The Ko criterion has shown an ability to predict fracture in both wire drawing processes [128] and in the hub-hole expanding process [132]. For the wire drawing, $\xi \approx 1.0$ at the wire centre, where fracture originates [128]. For this reason, the proposed function does not incorporate a dependency on ξ, and final expression for S takes the form

$$S(\eta) = \frac{2S_0}{(1.0 + 3\eta)} \tag{33}$$

Crack Closure Effects

An additional limitation of the classic Lemaitre damage model is that it does not distinguish between tensile and compressive stress states, whereas it is known from experiments that tensile stresses are considerably more conducive to crack growth than compressive stresses [98]. To overcome this shortcoming, some authors assume no crack growth in compressive stress states [99]; however, this does not account for the partial closure of micro-defects under compressive stress states.; this effect causes a greater material area to bear the compressive load. As a result, the material may exhibit a partial or complete recovery of its stiffness, depending on the specific conditions [100]. This approach also does not account for the fact that some crack growth can occur in compressive stages [25].

Consequently, an *enhanced* Lemaitre model with crack closure effects has been proposed [100, 101]. In this approach, the energy release rate Y (Equation 30) is rewritten to account for the differing contributions of tensile and compressive stresses:

$$\begin{aligned} Y \;=\; & \frac{-1}{2E\,(1-D)}\left[(1+\nu)\boldsymbol{\sigma}^{+} : \boldsymbol{\sigma}^{+} - \nu\,\langle \mathrm{tr}(\boldsymbol{\sigma})\rangle^{2}\right] \\ & - \frac{h}{2E\,(1-hD)}\left[(1+\nu)\boldsymbol{\sigma}^{-} : \boldsymbol{\sigma}^{-} - \nu\langle -\mathrm{tr}(\boldsymbol{\sigma})\rangle^{2}\right] \end{aligned} \tag{34}$$

where Macaulay brackets are indicated by $\langle \bullet \rangle$. The parameter $0 \leq h \leq 1$ accounts for the crack closure phenomenon; here, we take $h = 0.2$ as is common for steels [86, 102, 103]). The positive and negative stress components are defined as

$$\boldsymbol{\sigma}^{+} = \sum_{i=1}^{3} \langle \sigma_i \rangle \mathbf{e}_i \otimes \mathbf{e}_i \tag{35}$$

$$\boldsymbol{\sigma}^{-} = \sum_{i=1}^{3} \langle -\sigma_i \rangle \mathbf{e}_i \otimes \mathbf{e}_i \tag{36}$$

where σ_i are the principal stresses, $\{\mathbf{e}_1, \mathbf{e}_2, \mathbf{e}_3\}$ are the orthonormal basis vectors, and $\boldsymbol{\sigma} = \boldsymbol{\sigma}^{+} + \boldsymbol{\sigma}^{-}$.

A simplified form of the crack-closure model [100] is employed in this work, whereby this definition of decomposed stress is only used in the damage evolution calculation.

Non-Local Damage

One limitation of damage models is that due to the strain softening behaviour, prediction may suffer from mesh size and orientation dependency in localised strain zones [95–97]. To rectify this, an implicit *non-local* damage variable $\bar{D}$ is introduced as in Peerlings et al. [95, 96] and Geers et al.

[97]. This is related to the local damage variable D through the implicit diffusion equation:

$$\bar{D} - l_c^2 \boldsymbol{\nabla}^2 \bar{D} = D \tag{37}$$

where l_c is a characteristic length scale which controls the area over which the local damage is diffused. This equation can be viewed as a smoothing equation ($\bar{D}$ is a spatially smoothed version of D), which has the effect of mitigating the mesh dependency. This equation is solved with the zero-flux Neumann boundary conditions on all boundaries: $\boldsymbol{n} \cdot \nabla \bar{D} = 0$. The terms in Equation 37 are discretised using the cell-centred finite volume method, similar to the pressure equation (Equation 14).

3.4.2 Computational Procedure

An implicit-explicit algorithm is developed in this work to solve Equations 27-29. At every outer iteration, the plastic increment is solved implicitly, with the value for the damage variable fixed from the previous outer iteration. The damage rate equation (Equation 29) is then solved in a *deferred-correction* manner using the damage from the previous iteration ($\bar{D}_{[i]}$, where $[i]$ indicate a value from a previous outer iteration). This approach avoids the use of a 2×2 matrix (or an even higher dimension matrix if one was to solve for anisotropic plasticity or plasticity incorporating kinematic hardening) that would be needed if both the damage and the plastic increment were solved for implicitly simultaneously. By not requiring the solution of both the plasticity and damage simultaneously, the mathematics are simplified when solving for more complex formulations of the Lemaitre damage evolution equation and for the *non-local damage*, which will be described later in this section. Note that the overall solution algorithm is still implicit in time.

This stress calculation procedure for the Lemaitre damage model is summarised in Algorithm 3, where $\bar{D}_{[i]}^{[m+1]}$ is the latest available non-local damage field at the new time, i.e. its values from the previous outer iteration; at convergence within each time step, $\bar{D}_{[i]}^{[m+1]}$ becomes $\bar{D}_{[i+1]}^{[m+1]} \equiv \bar{D}^{[m+1]}$. As shown, to aid numerical convergence, a critical damage parameter D_c is incorporated [72], which limits the maximum value of the damage D to D_c, rather than 1. In the current work, $D_c = 0.99$ is assumed. Consequently, the damage rate equation (Equation 30) becomes

$$\dot{D} = \begin{cases} 0 & \text{if } \eta \leq -\frac{1}{3} \text{ or } D \geq D_c \\ \frac{\dot{\bar{\varepsilon}}_p}{1-D} \left(\frac{-Y}{S(\eta,\xi)} \right)^b & \text{if } \eta > -\frac{1}{3} \text{ and } D < D_c \end{cases} \tag{38}$$

where S can be a function of η and ξ as described above.

Although subtle, we have found that limiting the value of the non-local damage field $\bar{D}$ (step (viii)) is critical for achieving reliable predictions. This step prevents nonphysical behaviour whereby a cell that is set as being fully damaged ($D = D_c$) is contributing to the damage growth in the surrounding cells through the non-local damage field.

Algorithm 3: Lemaitre damage model stress calculation algorithm

(i) Update deformation gradients for a given incremental displacement

$$\mathbf{f}^{[m+1]} = \mathbf{I} + [\boldsymbol{\nabla}(\Delta\mathbf{u})]^T$$

$$\mathbf{F}^{[m+1]} = \mathbf{f}^{[m+1]} \cdot \mathbf{F}^{[m]}$$

(ii) Compute trial elastic state

$$\mathbf{B}_e^{[m]} = \exp\left(2\boldsymbol{\varepsilon}_e^{[m]}\right)$$

$$\mathbf{B}_e^{\text{trial}} = \mathbf{f}^{[m+1]} \cdot \mathbf{B}_e^{[m]} \cdot (\mathbf{f}^{[m+1]})^T$$

$$\boldsymbol{\varepsilon}_e^{\text{trial}} = \frac{1}{2}\ln(\mathbf{B}_e^{\text{trial}})$$

$$\bar{\varepsilon}_p^{\text{trial}} = \bar{\varepsilon}_p^{[m]}$$

$$\sigma_v^{\text{trial}} = \sqrt{3/2}||2G \text{ dev}(\boldsymbol{\varepsilon}_e^{\text{trial}})||$$

Andrew: should the yield function include D old (equation 26)?

$$\Phi^{\text{trial}} = \sigma_v^{\text{trial}} - \sigma_y(\bar{\varepsilon}_p^{\text{trial}})$$

if $\Phi^{trial} > 0$ **then**
  go to step (iii) to solve for $\Delta\bar{\varepsilon}_p$
else
  $\Delta\bar{\varepsilon}_p = 0$ and go to step (iv)
end

(iii) Use the Newton-Raphson method to solve the yield function for $\Delta\bar{\varepsilon}_p$:

$$\sigma_v^{\text{trial}} - \frac{3\mu\Delta\bar{\varepsilon}_p}{1 - \bar{D}_{[i]}^{[m+1]}} - \sigma_y(\bar{\varepsilon}_p^{[m]} + \Delta\bar{\varepsilon}_p) = 0$$

(iv) Update constitutive variables and deviatoric stress

$$\boldsymbol{\varepsilon}_e^{[m+1]} = \boldsymbol{\varepsilon}_e^{\text{trial}} - \sqrt{\frac{3}{2}}\frac{\Delta\bar{\varepsilon}_p}{1 - \bar{D}_{[i]}^{[m+1]}}\frac{\text{dev}(\boldsymbol{\varepsilon}_e^{\text{trial}})}{||\boldsymbol{\varepsilon}_e^{\text{trial}}||}$$

$$\bar{\varepsilon}_p^{[m+1]} = \bar{\varepsilon}_p^{[m]} + \Delta\bar{\varepsilon}_p$$

$$\boldsymbol{s}^{[m+1]} = \left(1 - \bar{D}_{[i]}^{[m+1]}\right)(1/J)2\mu \text{ dev}\left(\boldsymbol{\varepsilon}_e^{[m+1]}\right)$$

(v) Implicitly solve the pressure Poisson's equation, where $J^{[m+1]} = -(1 - \bar{D}_{[i]}^{[m+1]})\kappa \text{ tr}\left(\boldsymbol{\varepsilon}_e^{[m+1]}\right)$.

$$p^{[m+1]} - \mathbb{D}\boldsymbol{\nabla}^2 p^{[m+1]} = -\frac{\kappa}{2}\left[\left(J^{[m+1]}\right)^2 - 1\right] - \boldsymbol{\nabla}\cdot\left(\mathbb{D}\boldsymbol{\nabla}p_{[i]}^{[m+1]}\right) \tag{39}$$

(vi) Update the true (Cauchy) stress

$$\boldsymbol{\sigma}^{[m+1]} = \boldsymbol{s}^{[m+1]} - p^{[m+1]}\mathbf{I}$$

(vii) Update the local damage (use the modified form for Y if the crack $h > 0$)

$$D^{[m+1]} = \begin{cases} D^{[m]} & \text{if } \eta \leq -\frac{1}{3} \text{ or } D_{[i]}^{[m+1]} \geq D_c \\ \max\left[D^{[m]} + \frac{\dot{\bar{\varepsilon}}_p}{1-D_{[i]}^{[m+1]}}\left(\frac{-Y}{S(\eta,\xi)}\right)^b,\ D_c\right] & \text{if } \eta > -\frac{1}{3} \text{ and } D_{[i]}^{[m+1]} < D_c \end{cases} \tag{40}$$

(vii) Implicitly solve diffusion equation for non-local damage

$$\bar{D}^{[m+1]} - l_c^2\boldsymbol{\nabla}^2\bar{D}^{[m+1]} = D^{[m+1]} \tag{41}$$

(viii) Limit the non-local damage

$$\bar{D}^{[m+1]} = \max\left(\bar{D}^{[m+1]}, D_c\right) \tag{42}$$

3.5 Gurson-Tvergaard-Needleman Model

3.5.1 Model Formulation

Gurson [74] proposed the canonical micro-mechanical framework for ductile damage prediction and provides the basis for various derived models [10, 14, 104**?**]. This model posits the existence of micro-voids in the material. The density of these voids is described by a variable denoted as porosity. The material degradation is characterised by the increasing porosity due to these voids' growth. Gurson's framework was further developed by Tvergaard and Needleman [75] to account for the void nucleation and coalescence, leading to the Gurson-Tvergaard-Needleman (GTN) model.

Andrew: check signs, assuming $p = -tr(\sigma)/3$
Andrew: should f be f_* in the 2nd eqn?
The GTN model is described by a yield equation, flow rule (deviatoric and volumetric), consistency condition, and porosity evolution equations:

$$\Phi = \left(\frac{\sigma_v}{\sigma_y}\right)^2 + 2q_1 f_* \cosh\left(\frac{3q_2 p}{2\sigma_y}\right) - \left(1 + q_3 f_*^2\right) \tag{43}$$

$$\dot{\bar{\varepsilon}}_p = \frac{1}{(1-f)\sigma_y}(\sigma_v \dot{\bar{\varepsilon}}_{\text{dev}} - p\dot{\bar{\varepsilon}}_{\text{vol}}) \tag{44}$$

$$\dot{\bar{\varepsilon}}_{\text{vol}} \frac{\partial \Phi}{\partial \sigma_v} + \dot{\bar{\varepsilon}}_{\text{dev}} \frac{\partial \Phi}{\partial p} = 0 \tag{45}$$

$$\dot{f} = (1-f)\,\text{tr}\,(\dot{\boldsymbol{\varepsilon}}_p) + A\dot{\bar{\varepsilon}}_p \tag{46}$$

where q_1, q_2 and q_3 are dimensionless material parameters. The effective void fraction f_*, which accounts for void coalescence, is

$$f_* = \begin{cases} f & \text{if } f \leq f_c \\ f_c + (f - f_c)\,\frac{f_u - f_c}{f_f - f_c} & \text{if } f > f_c \end{cases} \tag{47}$$

where f is the porosity, f_c is the void volume fraction at which void coalescence begins, f_u is the ultimate volume fraction, and f_f is the volume fraction at fracture.

The rate of volumetric plastic strain and equivalent deviatoric plastic strain are given, respectively, by

$$\dot{\boldsymbol{\varepsilon}}_{\text{vol}} = \dot{\bar{\varepsilon}}_p \frac{\partial \phi}{\partial p} \tag{48}$$

$$\dot{\boldsymbol{\varepsilon}}_{\text{dev}} = \dot{\bar{\varepsilon}}_p \frac{\partial \phi}{\partial \sigma_v} \tag{49}$$

The dimensionless coefficient A is chosen to ensure void nucleation follows a normal distribution [99]:

$$A = \begin{cases} \frac{f_n}{S_n\sqrt{2\pi}} \exp\left[-\frac{1}{2}\left(\frac{\bar{\varepsilon}_p - \varepsilon_n}{S_n}\right)\right] & \text{if } p < 0 \\ 0 & \text{if } p \geq 0 \end{cases} \tag{50}$$

where f_n determines the total void fraction possible, ε_n is the mean nucleation strain, and S_n is the nucleation strain standard deviation.

Lode Angle Dependence

Further developments of the GTN model have been made to better account for fracture in stress states with significant shearing [77, 105–107]. This work adopts the expression developed by Nahshon and Hutchinson [77] for shearing-related void growth, which has shown an ability to accurately predict fracture in the blanking metal forming process [105]. The porosity evolution equation

(Equation) is consequently replaced by where

$$\dot{f} = (1 - f)\,\mathrm{tr}\,(\dot{\boldsymbol{\varepsilon}}_p) + A\dot{\bar{\varepsilon}}_p + k_w f \frac{1 - \xi^2}{\sigma_v}\,\mathrm{dev}(\boldsymbol{\sigma}) : \dot{\boldsymbol{\varepsilon}}_p \tag{51}$$

Non-Local Porosity

Like the Lemaitre model, mesh dependency in the GTN model can be mitigated by introducing non-local damage variables [107, 108]. In the case of the GTN model, a non-local porosity variable is determined using a non-local gradient (smoothing) equation:

$$\bar{f} - {l_c}^2 \boldsymbol{\nabla}^2 \bar{f} = f \tag{52}$$

where $\bar{f}$ is the non-local (smoothed) porosity field. This equation can be discretised, as before, using the described cell-centred finite volume method and zero-flux Neumann boundary conditions.

3.5.2 Computational Procedure

Philip reminder: make notation consistent for tensor multiplication

For the GTN model, the elastoplasticity stress calculation is extended to determine porosity f in addition to stress and plastic strain. The adopted computational algorithm is shown in Algorithm 4. As in the Lemaitre computational procedure, we propose an explicit-implicit algorithm to solve the system of equations: Equations 43, 44 and 45 are solved implicitly for the variables $\varepsilon_{\mathrm{vol}}$, $\varepsilon_{\mathrm{dev}}$ and $\bar{\varepsilon}_p$ using a Newon-Raphson method, while the porosity f (Equation 3.5.1) is calculated in a deferred-correction/explicit manner. Once again, the overall procedure is implicit in time.

3.6 Phase field fracture model

3.6.1 Model Formulation

In recent years, phase field approaches have received much attention for the prediction of fracture and failure [19–23, 109, 110], showing an ability to predict complex crack patterns, including branching and merging in both two and three dimensions [109, 110]. In this method, sharp cracks are *regularised* over a continuum, leading to a system of partial differential equations that are relatively simple to implement in finite element, finite volume and related solvers.

The phase field method for damage, initially proposed by Francfort and Marigo [111] to describe brittle fracture, is based on a variational approach to minimise a Griffiths theory potential energy functional. This approach leads to a Mumford-Shah [112] type energy potential that can be approximated by a phase-field formulation following the work of Ambrosio and Tortorelli [113]. This approximation was adopted by Bourdin et al. [114] to facilitate numerical solutions of the variational formulation, and further extended by Miehe et al. [110] who derived the phase field approach

Algorithm 4: GTN damage model stress calculation algorithm

(i) Update deformation gradients for a given incremental displacement

$$\mathbf{f}^{[m+1]} = \mathbf{I} + \nabla\left[\Delta\mathbf{u}\right]^T$$
$$\mathbf{F}^{[m+1]} = \mathbf{f}^{[m+1]}\mathbf{F}_n$$

(ii) Compute trial elastic state

$$\mathbf{B}_e^{[m]} = \exp\left(2\boldsymbol{\varepsilon}_e^{[m]}\right)$$
$$\mathbf{B}_e^{\text{trial}} = \mathbf{f}^{[m+1]}\mathbf{B}_e^{[m]}(\mathbf{f}^{[m+1]})^T$$
$$\boldsymbol{\varepsilon}_e^{\text{trial}} = \frac{1}{2}\ln[\mathbf{B}_e^{\text{trial}}]$$
$$p^{\text{trial}} = \kappa\,\text{tr}(\boldsymbol{\varepsilon}_e^{\text{trial}})$$
$$\mathbf{s}^{\text{trial}} = 2\mu\,\text{dev}(\boldsymbol{\varepsilon}_e^{\text{trial}})$$
$$\sigma_v^{\text{trial}} = \sqrt{3/2}||2\mu\,\text{dev}(\boldsymbol{\varepsilon}_{\text{trial}}^e)||$$
$$\mathbf{n} = \frac{3}{2}\frac{\mathbf{s}^{\text{trial}}}{\sigma_v^{\text{trial}}}$$
$$\Phi^{\text{trial}} = \left(\frac{\sigma_v^{\text{trial}}}{\sigma_y}\right)^2 + q_1 f_{*[i]}^{[m+1]}\cosh\left(\frac{3q_2 p^{\text{trial}}}{2\sigma_y}\right) - \left(1 + q_3 {f_{*[i]}^{[m+1]}}^2\right)$$

if $\Phi^{trial} > 0$ **then**
| go to step (iii)
else
| set $\Delta\varepsilon_{\text{vol}} = \Delta\varepsilon_{\text{dev}} = \Delta\bar{\varepsilon}_p = 0$ and $\Delta\boldsymbol{\varepsilon}_p = \mathbf{0}$. Go to step (iv)
end

(iii) Enter small strain return map and solve the system of equations (equation **??**) for $\Delta\varepsilon_h^{[m+1]}$, $\Delta\varepsilon_q^{[m+1]}$ and $\Delta\bar{\varepsilon}^p_{[m+1]}$

(iv) Update the constitutive variables

$$\bar{\varepsilon}_p^{[m+1]} = \bar{\varepsilon}_p^{[m]} + \Delta\bar{\varepsilon}_p$$
$$\boldsymbol{\varepsilon}_p^{[m+1]} = \boldsymbol{\varepsilon}_p^{[m]} + \Delta\boldsymbol{\varepsilon}_p$$
$$\boldsymbol{\varepsilon}_e^{[m+1]} = \boldsymbol{\varepsilon}^{\text{trial}} - (1/3)\Delta\varepsilon_{\text{vol}}^{[m+1]}\,\mathbf{I} - \Delta\varepsilon_{\text{dev}}^{[m+1]}\,\mathbf{n}$$
$$\boldsymbol{s}^{[m+1]} = \frac{1}{J}\left[2/3\left(\sigma_v^{\text{trial}} - 3\mu\Delta\varepsilon_{\text{dev}}^{[m+1]}\right)\mathbf{n}\right]$$

(v) Implicitly solve the pressure Poisson's equation:

$$p^{[m+1]} - \mathbb{D}\boldsymbol{\nabla}^2 p^{[m+1]} = \frac{1}{J}\left(p_{\text{trial}} - \kappa\Delta\varepsilon_{\text{vol}}^{[m+1]}\right) - \boldsymbol{\nabla}\cdot\left(\mathbb{D}\boldsymbol{\nabla}p_{[i]}^{[m+1]}\right) \tag{53}$$

(vi) Update the true (Cauchy) stress

$$\boldsymbol{\sigma}^{[m+1]} = \boldsymbol{s}^{[m+1]} - p^{[m+1]}\mathbf{I}$$

(vii) Calculate the porosity $f_{[i+1]}^{[m+1]}$ and the effective porosity $f_{*[i+1]}^{[m+1]}$:

$$f^{[m+1]} = f^{[m]} + \left(1 - f_{[i]}^{[m+1]}\right)\text{tr}\left(\dot{\boldsymbol{\varepsilon}}_p^{[m+1]}\right) + A\dot{\bar{\varepsilon}}_p^{[m+1]} + k_w f\frac{1-\xi^2}{\sigma_v^{[m+1]}}\text{dev}(\boldsymbol{\sigma}^{[m+1]}) : \dot{\boldsymbol{\varepsilon}}_p^{[m+1]} \tag{54}$$

$$f^{*[m+1]} = \begin{cases} f^{[m+1]} & \text{if } f^{[m+1]} \le f_c \\ f_c + \left(f^{[m+1]} - f_c\right)\frac{f_u - f_c}{f_f - f_c} & \text{if } f^{[m+1]} > f_c \end{cases} \tag{55}$$

(viii) Implicitly solve non-local porosity equation:

$$\bar{f}^{[m+1]} - l_c^2\boldsymbol{\nabla}^2\bar{f}^{[m+1]} = f^{[m+1]} \tag{56}$$

from continuum mechanics and thermodynamic arguments. Miehe et al. [110] also added an important mechanism for distinguishing between tensile and compressive effects on crack growth, as well as including a history variable $\mathcal{H}$ which ensures the irreversibility of crack growth. Several studies have shown the ability of these models to produce results consistent with benchmark fracture cases [109, 110].

The phase field approach has since been extended to ductile fracture by Ambati et al. [19], Borden et al. [20] and Miehe et al. [21]. The approach from Ambati et al. [19] involves incorporating a plastic strain dependency in the elastic degradation function while the approach from Miehe et al. [21] incorporates the plastic strain energy into the crack driving variable $\mathcal{H}$. Borden et al. [20] uses a similar approach to Miehe et al. [21] by incorporating the plastic strain into the crack driving variable $\mathcal{H}$ while also introducing a plastic degradation function to ensure that fracture is preceded by large plastic strains, as is the case experimentally.

In this work, the approach form Borden et al. [20] is chosen to be most suitable, given the large plastic strains expected in wire drawing. The strong form of the phase field equation is given by:

$$\frac{G_c}{2l}\left(d - 4l^2\boldsymbol{\nabla}^2 d\right) = \mathcal{H} \tag{57}$$

where $0 < d \leq 1$ is the damage variable, with $d = 0$ characterising the unbroken state and $d = 1$ characterising the fully broken state. The variable d is conceptually similar to the damage variable D used in the Lemaitre and GTN damage mechanics, with d being a macroscopic variable that characterises the growth of micro-voids and micro-cracks. The critical fracture energy per unit area is given by G_c. The parameter l is a length-scale variable that regularises the crack surface. It is typically chosen as a function of the local element/cell size. The crack driving variable $\mathcal{H}$ is

$$\mathcal{H} = -2d\max\left[\psi_e\left(\boldsymbol{\varepsilon}^e\right), \bar{\psi}_e\left(\boldsymbol{\varepsilon}^e\right)\right] - 2d\langle\psi_p(\bar{\varepsilon}^p) - w_0\rangle \tag{58}$$

where $\psi_e\left(\varepsilon^e\right)$ is the current elastic energy contribution, $\bar{\psi}_e\left(\varepsilon^e\right)$ is a history variable which gives the largest value reached by the elastic energy contribution in time, The elastic energy contribution $\psi_e\left(\varepsilon^e\right)$ is decomposed into positive and negative components, such that only positive elastic strain energy contributes towards the crack driving energy [115]:

$$\begin{aligned}
\psi_e &= \left(1 - d^2\right)\psi_e^+\left(\boldsymbol{\varepsilon}_e\right) + \psi_e^-\left(\boldsymbol{\varepsilon}_e\right) && (59)\\
\psi_e^+\left(\boldsymbol{\varepsilon}^e\right) &= \frac{\kappa}{2}\langle\mathrm{tr}\left(\boldsymbol{\varepsilon}_e\right)\rangle^2 + \mu\,\mathrm{dev}(\boldsymbol{\varepsilon}_e) : \mathrm{dev}(\boldsymbol{\varepsilon}_e) && (60)\\
\psi_e^-\left(\boldsymbol{\varepsilon}_e\right) &= \frac{\kappa}{2}\langle-\mathrm{tr}\left(\boldsymbol{\varepsilon}_e\right)\rangle^2 && (61)
\end{aligned}$$

The plastic energy contribution to the crack growth $\psi_p\left(\bar{\varepsilon}^p\right)$ is given by [117]:

$$\psi_p(\bar{\varepsilon}^p) = \int_0^{\bar{\varepsilon}^p} \sigma_y \, d\bar{\varepsilon}^p \tag{62}$$

and w_0 is the plastic work threshold, below which the plastic strain will not contribute to crack growth.

Finally, the isotropic J_2 yield function (Equation 22) is modified as [20]

$$\Phi = \sigma'_v \; - \; (1 - d^2)\, \sigma_y\, (\bar{\varepsilon}_p) \tag{63}$$

where

$$\sigma'_v \; = \; \sqrt{3/2\, \boldsymbol{s}' : \boldsymbol{s}'} \tag{64}$$

$$\boldsymbol{s}' \; = \; (1 - d^2)\, 2\mu\, \mathrm{dev}\, (\boldsymbol{\varepsilon}_e) \tag{65}$$

In this work, the phase field equation (Equation 57) is discretised using the described cell-centred finite volume method, and zero-flux Neumann boundary conditions $\boldsymbol{n} \cdot \nabla d = 0$ are used for all boundaries.

3.6.2 Computational Procedure

Similar to the Lemaitre and GTN procedures, a deferred-correction procedure is adopted here for incorporation of the phase (damage) evolution equation. Within each outer iteration, the elastoplastic quantities are calculated using the latest available phase field variable $d^{[m+1]}_{(i)}$ from the previous outer iteration i. Subsequently, the phase field equation (Equation 57) is solved using the latest available stress and strain fields. The algorithm for the phase field stress calculation procedure is given in Algorithm 5.

Andrew: check equations

Algorithm 5: Phase field damage model stress calculation algorithm

(i) Update deformation gradients for a given incremental displacement

$$\mathbf{f}^{[m+1]} = \mathbf{I} + \nabla [\Delta \mathbf{u}]^T$$
$$\mathbf{F}^{[m+1]} = \mathbf{f}^{[m+1]} \mathbf{F}_n$$
$$J^{[m+1]} = \det \left(\mathbf{F}^{[m+1]} \right)$$

(ii) Compute trial elastic state

$$\mathbf{B}_e^{[m]} = \exp \left(2\boldsymbol{\varepsilon}_e^{[m]} \right)$$
$$\mathbf{B}_e^{\text{trial}} = \mathbf{f}^{[m+1]} \mathbf{B}_e^{[m]} \left(\mathbf{f}^{[m+1]} \right)^T$$
$$\boldsymbol{\varepsilon}_e^{\text{trial}} = \frac{1}{2} \ln \left(\mathbf{B}_e^{\text{trial}} \right)$$
$$\sigma_v^{\text{trial}} = \left(1 - d_{[i]}^{[m+1]2} \right) \sqrt{\frac{3}{2}} ||2\mu \operatorname{dev}(\boldsymbol{\varepsilon}_e)||$$
$$\Phi^{\text{trial}} = \sigma_v^{\text{trial}} - \left(1 - d_{[i]}^{[m+1]2} \right) \sigma_y \left(\bar{\varepsilon}_p^{[m]} \right)$$

if $\Phi_{trial} > 0$ **then**
| go to step (iii) to solve for $\Delta \bar{\varepsilon}_p$
else
| $\Delta \bar{\varepsilon}_p = 0$ and go to step (iv)
end

(iii) Use the Newton-Raphson to solve the yield equation for the equivalent plastic strain increment $\Delta \bar{\varepsilon}_p$:

$$\sigma_v^{\text{trial}} - \left(1 - d_{[i]}^{[m+1]2} \right) 3\mu \Delta \bar{\varepsilon}_p - \left(1 - d_{[i]}^{[m+1]2} \right) \sigma_y (\bar{\varepsilon}_p^{[m]} + \Delta \bar{\varepsilon}_p) = 0$$

(iv) Update the constitutive variables

$$\boldsymbol{\varepsilon}_e^{[m+1]} = \boldsymbol{\varepsilon}_e^{\text{trial}} - \sqrt{3/2}\, \Delta \bar{\varepsilon}_p \frac{\operatorname{dev}(\boldsymbol{\varepsilon}_e^{\text{trial}})}{|||\boldsymbol{\varepsilon}_e^{\text{trial}}||}$$
$$\boldsymbol{s}^{[m+1]} = \left[1 - \left(d_{[i]}^{[m+1]} \right)^2 \right] (1/J)\, 2\mu \operatorname{dev} \left(\boldsymbol{\varepsilon}_e^{[m+1]} \right)$$
$$\bar{\varepsilon}_p^{[m+1]} = \bar{\varepsilon}_p^{[m]} + \Delta \bar{\varepsilon}_p$$

(v) Implicitly solve the pressure Poisson's equation:

$$p^{[m+1]} - \mathbb{D} \boldsymbol{\nabla}^2 p^{[m+1]} = -\frac{\kappa}{2} \left[\left(J^{[m+1]} \right)^2 - 1 \right] - \boldsymbol{\nabla} \cdot \left(\mathbb{D} \boldsymbol{\nabla} p_{[i]}^{[m+1]} \right) \tag{66}$$

(vi) Update the true (Cauchy) stress

$$\boldsymbol{\sigma}^{[m+1]} = \boldsymbol{s}^{[m+1]} - p^{[m+1]} \mathbf{I}$$

(vi) Solve the phase field equation for d:

$$\frac{G_c}{2l} \left(d^{[m+1]} - 4l^2 \boldsymbol{\nabla}^2 d^{[m+1]} \right) = \mathcal{H}_{[i]}^{[m+1]} \tag{67}$$

4 Benchmark Cases

This section assesses the performance of the developed finite volume procedures on two benchmark test cases: (i) 2-D axisymmetric notched round bar and (ii) 3-D flat notched bar. In both test cases, a region of localised plastic straining develops at the centre of the specimen, but the levels of triaxiality experienced differ. The cases are presented simultaneously rather than sequentially to allow easier comparison of the material models.

Unless stated otherwise, a global Rhie-Chow scale factor $\mathcal{R} = 0.01$ is used in all of the following finite volume simulations. All simulations were run in parallel on eight CPU cores (Intel Xeon 6152).

Comparisons are made with predictions from finite element software Abaqus and results from the literature. In the Abaqus models, linear interpolation functions are used in the finite element simulations (Abaqus element code C3D8T for 3-D and CAX4RT for axisymmetry). For reference, single-cell verifications of the proposed material models are provided in Appendix A, providing confidence that the constitutive laws are implemented as intended.

4.1 Geometries and Meshes

The notched round bar (Figure 4.1) has been widely used for benchmarking plasticity and damage procedures [118–120]. The geometry consists of a 40 mm long round bar of diameter 18 mm with a 4 mm rounded notch. A 2-D axisymmetric model is created, including a horizontal symmetry plane, and a structured quadrilateral mesh is employed (Figure 4).

./Figures/finiteVolumeImplementation/inhomogenousDeformation/axiNotched

Fig. 3 Geometry of the notched round bar

./Figures/finiteVolumeImplementation/inhomogenousDeformatio

Fig. 4 Notched round bar mesh (mesh with 100 cells)

The 3-D flat notched tensile specimen (Figure 4.1) is another common test case for assessing damage models [20, 121]. The geometry consists of 152.4 × 25.4 mm plate with 4.06 mm diameter side notches. The solution domain comprises one-eighth of the specimen by exploiting three symmetry planes. A structured hexahedral mesh is employed (Figure 6).

./Figures/finiteVolumeImplementation/inhomogenousDeformation/flatNotch

Fig. 5 Geometry of the flat notched bar

./Figures/finiteVolumeImplementation/inhomogenousDeformation

Fig. 6 Flat notched bar mesh (mesh with 1000 cells)

4.2 Loading Conditions

For the notched round bar case, a vertical displacement of 1.0 mm is quasi-statically applied to the upper boundary. For the elastoplastic cases without damage, a displacement increment size of 0.01 mm is used, whereas a smaller increment size of 0.001 mm is used for the cases with damage.

For the flat notched bar case, a vertical displacement of 1.143mm is quasi-statically applied to the upper boundary. In the elastoplastic cases, displacement increments of 0.01143 m are applied, and in the damage cases, displacement increments of 0.001143 m are applied.

An adaptive time-stepping procedure was employed for the Abaqus finite element cases, allowing a minimum displacement increment of 0.01143 mm.

4.3 Plasticity Model Verification

Before verifying the damage and fracture models, the implementation of the described plasticity model is verified by comparison with three other procedures:

(a) The approach of Clancy [11] implemented in OpenFOAM that uses the logarithmic strain and the Mandel stress [84];
(b) The approach of Cardiff et al. [13] implemented in OpenFOAM, which uses the Green strain tensor (left Cauchy–Green deformation tensor) and the return mapping algorithm described by Simo and Hughes [81];

(c) The default approach in Abaqus, which is based on the Jaumann stress rate.

Verification consists of examining the reaction forces at the loading boundary and the equivalent plastic strain $\bar{\varepsilon}_p$, equivalent stress σ_v, hydrostatic pressure p and axial stress σ_{yy} (stress in the loading direction) at the centre of the specimen (location of the maximum equivalent plastic strain and where fracture will initiate when damage models are incorporated).

The mesh spacing and time-step size are chosen so that spatial and temporal discretisation are small for all cases.

4.3.1 Material Parameters

The elastoplastic material parameters for the notched round bar are given in Table 1, while the parameters for the flat notched bar are given in Table 2.

Property	Symbol	Value	Units
Young's modulus	E	69	GPa
Poisson's ratio	v	0.3	-
Hardening law	σ_y	$589(10^{-4} + \bar{\varepsilon}_p)^{0.216}$	MPa

Table 1 Material properties for the notched round bar case

Property	Symbol	Value	Units
Young's modulus	E	68.8	GPa
Poisson's ratio	v	0.33	-
Hardening law	σ_y	$320 + 688\bar{\varepsilon}_p$	MPa

Table 2 Material properties for the flat notched bar case

4.3.2 Reaction Forces

The predicted reaction forces at the loading boundaries (Figures 7) align closely between all approaches. It is worth noting that the reaction forces for both the Clancy [11] implementation and the implementation of this work (which both use the logarithmic strain) are slightly less than the Cardiff et al. [13] and the Abaqus predictions in the latter stages of the deformation. Although the reason for these subtle differences is unclear, the lack of mathematical equivalence between the logarithmic and Green/Jaumann strain approaches may be the cause.

(a) Notched round bar

(b) Flat notched bar

Fig. 7 Reaction forces at the loading boundaries for the notched round bar and flat notched bar cases

4.3.3 Stresses and Strains

The equivalence plastic strain predictions at the specimen centres are shown to agree for all approaches (Figure 8). The predicted equivalent plastic strain is marginally greater in the latter stages of the deformation for the finite volume (OpenFOAM) simulations than the Abaqus ones. These differences have been found to remain as the mesh spacing and time step are reduced, ruling out discretisation error as the cause. A possible reason for the difference is the use of the Jaumann objective rate in Abaqus [122], in contrast to the logarithmic and Green strain approaches used in OpenFOAM.

(a) Notched round bar

(b) Flat notched bar

Fig. 8 Equivalent plastic strain at the specimen centres

The predictions for equivalent stress σ_v, hydrostatic pressure p, and axial stress (stress in the loading direction) σ_{yy} are shown to agree for the different approaches (Figure 9). Of particular note is the pressure distribution, which is smooth and does not show numerical oscillations, providing confidence in the proposed pressure smoothing approach (Section 2.2.2).

./Figures/plasticityCompare/disp_sigmaEq.png

./Figures/plasticityCompare/hardenCompare/disp_sigmaEq.

(a) Notched round bar: Equivalent stress σ_v vs displacement

(b) Flat notched bar: Equivalent stress σ_v vs displacement

./Figures/plasticityCompare/disp_Pressure.png

./Figures/plasticityCompare/hardenCompare/disp_Pressure

(c) Notched round bar: Pressure p vs displacement

(d) Flat notched bar: Pressure p vs displacement

./Figures/plasticityCompare/disp_sigmaYY.png

./Figures/plasticityCompare/hardenCompare/disp_sigmaYY.

(e) Notched round bar: Axial stress σ_{yy} vs displacement

(f) Flat notched bar: Axial stress σ_{yy} vs displacement

Fig. 9 Stress and Strain Quantities at the Centre of the notched round bar and flat notched bar specimens

4.4 Lemaitre model

Following on from the verification of the elastoplasticity procedure, the notched round and flat bar test cases are examined using the proposed damage models.

4.4.1 Material Parameters

The Lemaitre material parameters for the notched round bar, taken from César de Sá et al. [118], are given in Table 3, while the Lemaitre material parameters for the flat notched bar case are given in Table 4.

Property	Symbol	Value	Units
Young's modulus	E	69.9	GPa
Poisson's ratio	v	0.3	-
Damage denominator	S_0	1.1	MPa
Damage exponent	b	1.0	-
Characteristic length	l_c	0.6325	mm
Hardening law	σ_y	$589(10^{-4} + \bar{\varepsilon}_p)^{0.216}$	MPa

Table 3 Lemaitre material parameters for the notched round bar case

Property	Symbol	Value	Units
Young's modulus	E	68.9	GPa
Poisson's ratio	v	0.33	-
Damage denominator	S_0	0.5	MPa
Damage exponent	b	1.0	-
Characteristic length	l_c	0.6325	mm
Hardening law	σ_y	$320 + 688\,\bar{\varepsilon}_p$	MPa

Table 4 Lemaitre material parameters for the flat notched bar case

4.4.2 Reaction Forces

Comments on reaction forces for both cases.

./Figures/LemaitreCompare/borden/bordenDispForce.png

Fig. 10 Force vs. displacement

4.4.3 Stresses, Strains and Damage

The distribution of the non-local damage at a displacement of 0.6 mm in the OpenFOAM simulation is compared with the results provided in César de Sá et al. [118] in Figure 5.16. In both of these cases, the non-local damage reaches a maximum of ≈ 0.5; it is clear that in both of these simulations, the distribution of the damage over the specimen follows a similar pattern.

./Figures/LemaitreCompare/updated_deSaNonLocal.jpeg

(a) Results from [118]

./Figures/LemaitreCompare/nlDamageLemaitre.png

(b) OpenFOAM simulation

Fig. 11 Comparison of non-local damage distribution

Comparing the OpenFOAM and Abaqus predictions (Figure 5.17), the OpenFOAM simulation of the non-local gradient Lemaitre model localises at a slightly quicker rate than the Abaqus implementation. This has been encountered earlier in the comparison of the equivalent plastic strain in section 5.3.2. The marginally faster increase of the equivalent plastic strain and damage results in a slightly quicker loss of load-carrying capacity for the specimen, as shown in Figure 5.18.

./Figures/LemaitreCompare/axiCompare/1.1LemaitreCompare.png

Fig. 12 Force vs. displacement

./Figures/LemaitreCompare/axiCompare/disp_damageNonLocal.png

./Figures/LemaitreCompare/axiCompare/disp_EpsPEq.png

(a) Non-local damage vs.displacement (mm)

(b) Equivalent plastic strain vs. displacement

Fig. 13 Abaqus and OpenFOAM implementations comparison

Again, it can be observed that there are slightly quicker increases in the damage and equivalent plastic strain for the OpenFOAM simulation (Figure 5.20). It is worth noting that Abaqus struggles to converge in the rapid crack propagation stage of this simulation, with it requiring very small displacement increments until it eventually crashes after a total displacement of $0.463\ mm$. By contrast, no such issues were encountered with the OpenFOAM simulation.

4.4.4 Effect of the S_0 Parameter

Here, the simulations are repeated for different values of the material parameter S_0. As the value of S_0 increases, rapid crack propagation occurs later in the deformation process. The discrepancies between OpenFOAM and Abaqus simulations are larger the later in the deformation process that fracture occurs.

./Figures/LemaitreCompare/borden/disp_damageNonLocal.png

./Figures/LemaitreCompare/borden/disp_EpsPEq.png

(a) Displacement vs. non-local Damage

(b) Displacement vs. equivalent plastic strain

Fig. 14 Abaqus and OpenFOAM implementations comparison

./Figures/LemaitreCompare/borden/lemaitreBordenCompare.png

Fig. 15 Force vs. displacement for different values of S_0

4.5 GTN Model

4.5.1 Material Parameters

Property	Symbol	Value	Units
Young's modulus	E	69	GPa
Poisson's ratio	v	0.3	-
q_1	q_1	1.5	-
q_2	q_2	1	-
q_3	q_3	2.25	-
Initial porosity	f_0	0.002	-
Nucleation strain mean	ε_n	0.15	-
Nucleation strain standard deviation	S_n	0.08	-
Void volume fraction parameter	f_n	0.2	-
Hardening law	σ_y	$589(10^{-4}+\bar{\varepsilon}_p)^{0.216}$	MPa

Table 5 GTN material parameters for the notched round bar case

4.5.2 Reaction Forces

In Figure 5.22, it can be seen that the results align well. As with the simulations conducted with the Lemaitre model, quicker localisation can be observed. A feature of this test case is the sharp crack propagation (Figure 5.23). The Abaqus simulation has convergence issues and eventually crashes at a displacement of approximately 0.371. No such convergence issues were encountered with OpenFOAM. The superior convergence abilities of the OpenFOAM simulations are likely because of the segregated solution procedure. By contrast, the Abaqus simulations require the calculation of the tangent stiffness matrix. For elastoplastic damage models, plastic deformation influences the onset and progression of damage and vice versa. This interaction can result in a significant coupling in the tangent stiffness matrix, manifesting as non-trivial off-diagonal terms [56]. These terms can introduce convergence difficulties.

4.5.3 Stresses, Strains and Damage

`./Figures/GTNCompare/forceDispGTN.jpg`

Fig. 16 Force vs. displacement

./Figures/GTNCompare/epsilonPEq_GTN.jpg

./Figures/GTNCompare/displacement_porosity.jpg

(a) Porosity vs. displacement (b) Equivalent plastic strain vs. displacement

Fig. 17 Abaqus and OpenFOAM implementations comparison

4.6 Phase Field Model

4.6.1 Material Parameters

The material properties are given in Table 6.

Property	Symbol	Value	Units
Young's modulus	E	68.8	GPa
Poisson's ratio	v	0.33	-
Critical Fracture Energy	G_c	60×10^3	J/m^2
Plastic Threshold	W_o	1×10^7	MPa
Characteristic Length	l_c	0.3226	mm
Hardening law	σ_y	$320 + 688\,\bar{\varepsilon}_p$	MPa

Table 6 Phase field material parameters for the notched flat notched bar case

4.6.2 Reaction Forces

The predicted reaction forces (Figure 18) agree closely with those from Borden et al. [20] and Eldahshan et al. [121]. It is worth noting that the normalised stress reported by Borden et al. [20] before the rapid crack propagation is slightly lower than that obtained here and by Eldahshan et al. [121].

./Figures/phaseCompare.png

Fig. 18 Normalised stress vs normalised strain

4.6.3 Stresses, Strains and Damage

No comparisons in the thesis: check references to see what can be compared

5 Wire Drawing Simulations

In the previous section, the developed elastoplastic damage procedures were verified on benchmark cases. In this section, the procedures are applied to the wire drawing metal forming process. A schematic of the wire drawing process is given in Figure 19. The key parameters in the wire drawing

./Figures/SimulationAndAnalysis/modelCompare/drawingSchematic.png

Fig. 19 Schematic of the wire drawing process

process are the die semi-angle α (°), which is the angle made by the die with the wire axis, and the reduction ratio r (%) is given by

$$r = 100 \times \left(\frac{d_i^2 - d_o^2}{d_i^2} \right) \tag{68}$$

where D_i is the wire initial diameter and D_o is the die of outlet diameter.

In the current cases, the entire length of the wire starts at the initial diameter, resulting in an overlap with the die. In the first time step, the contact procedure ‘pushes’ the wire back, enforcing the contact constraints. This procedure has been found to be efficient for quickly reaching quasi-steady-state drawing conditions; however, this approach can lead to convergence issues when incorporating damage, particularly in cases with large reduction ratios and high die angles. this issue is ameliorated by allowing the damage to evolve only after a user-specified time.

./Figures/SimulationAndAnalysis/wireMesh_InletOutlet.jpg

Fig. 20 Process for cell layer addition and removal

./Figures/SimulationAndAnalysis/initialContact.png

(a) Initial contact at first time step

./Figures/SimulationAndAnalysis/settledEpsilonPEq.png

(b) Equivalent plastic strain after 30 mm displacement

./Figures/SimulationAndAnalysis/settledDamage.png

(c) Damage after 30 mm displacement

Fig. 21 Wire drawing simulation

./Figures/SimulationAndAnalysis/damageIssue.png

Fig. 22 Issue with incorporating damage at initial stages of case

5.1 Comparison of damage and fracture models

In the wire drawing process, fracture typically originates in the centre of the specimen [124–127]. In this section, simulations are conducted for a typical wire drawing pass, with a reduction ration r of 10% and a drawing semi-angle α of 6° [128]. The wire drawing simulations were performed in serial on the UCD Sonic High Performance Computing (HPC) cluster.

The loading conditions and material parameters used are given in Tables 7.1-7. The material parameters for the die are taken from Clancy [11]. The elasto-plastic parameters of the wire used are similar to the ones that will be calibrated in section 7.3 for high-carbon steel. For the Lemaitre model with crack-closure effects, the crack-closure parameter is taken to be 0.2, as is typically the case for steels [86, 102, 103]. Aside from this, the parameters taken for the GTN, phase field and Lemaitre damage model are somewhat arbitrary and are mainly chosen for illustrative purposes. The values of these parameters will not affect the area of the wire where damage or fracture is predicted to occur but rather the level of damage or porosity that accumulates.

Quantity	Symbol	Value	Unit
Applied total displacement	u	30	mm
Time step	Δt	0.001	s
Displacement increment	Δu	0.2	mm
Friction coefficient	μ	0.1	-

Table 7 Loading conditions for wire drawing case

Quantity	Symbol	Value	Unit
Die inlet diameter		16	mm
Die outer diameter		20	mm
Die outlet Diameter		12.33	mm
Die semi-angle		6	°
Wire length		30	mm
Initial wire diameter		13	mm
Die cell size		0.4	mm
Wire cell size		0.4	mm

Table 8 Die and wire geometry

Term	Value	Units
Young's modulus	200	GPa
Poisson's ratio	0.3	-
Hardening law	$689 + (1340 - 689 + 250\,\bar{\varepsilon}_p)(1 - e^{-32.82\,\bar{\varepsilon}_p})$	MPa

Table 9 Wire elasto-plastic material parameters

Term	Value
Young's modulus	600 GPa
Poisson's ration	0.22

Table 10 Die material parameters

5.1.1 Lemaitre model

Property	Symbol	Value
Lemaitre damage denominator	S_0	13.5 MPa
Lemaitre damage exponent	b	1.0
Crack closure parameter	h	0.2

Table 11 Lemaitre model parameters

Simulations are here conducted for the Lemaitre damage model both with and without crack-closure effects. The resultant damage distributions are provided in Figures 7.5 and 7.6.

In Figure 7.5 (a), it can be observed that without crack-closure effects, the Lemaitre model gives a somewhat unrealistic damage distribution with damage being at a maximum away from the centre of the wire. This is due to the fact that it does not distinguish between positive and negative triaxialities. As a consequence of the triaxiality cut-off $\left(-\frac{1}{3}\right)$ for damage evolution, there is limited damage evolution towards the upper area of the wire.

By contrast, for the Lemaitre model with crack-closure effects, the damage is at a maximum at the centre of the bar. This is due to the fact that this is where the triaxiality, and relatedly the positive stress tensor τ^+, are at a maximum (Figure 7.6).

./Figures/SimulationAndAnalysis/modelCompare/classicLemaitre.png

(a) Damage distribution

./Figures/SimulationAndAnalysis/modelCompare/classsicLemaitreTriaxiality.pn

(b) Triaxiality distribution

Fig. 23 Lemaitre damage model without crack-closure effects

./Figures/SimulationAndAnalysis/modelCompare/crackClosureDamage.png

(a) Damage distribution

./Figures/SimulationAndAnalysis/modelCompare/crackClosureTauPositive.png

(b) Positive stress tensor distribution

Fig. 24 Lemaitre damage model with crack-closure effects

5.1.2 GTN model

Property	Symbol	Value
q1	$q1$	1.5
q2	$q2$	1
q3	$q3$	2.25
Initial porosity	f_0	0.002
Mean	ε_n	0.03
Standard deviation	S_n	0.02
Volume fraction	f_N	0.04

Table 12 GTN model parameters

./Figures/SimulationAndAnalysis/modelCompare/gtnModel.png

Fig. 25 Porosity distribution

For the GTN model, porosity growth is negligible for typical wire drawing passes [129] making void nucleation the dominant mechanism driving the evolution of the porosity. The GTN model accurately predicts the porosity to be at maximum at the centre of the wire. This is a consequence of the fact that porosity evolution due to nucleation is only set to occur when the pressure is positive (equation 50).

There are apparent issues with the assumption of the Gaussian distribution for void nucleation, however. To illustrate this, the evolution of the equivalent plastic strain and porosity is shown in Figure 7.8 for the cell at the centre of the wire and which has a cell-centre 0.3047 mm to the right of the wire inlet at the initial time step. The evolution of these variables is only displayed while this cell is in the process zone i.e. the region where it undergoes plastic straining. It can be observed that the Gaussian assumption leads to the porosity asymptoting towards a certain value, after which it does not evolve. This is unlikely to be a true reflection of the material behaviour [129].

./Figures/SimulationAndAnalysis/modelCompare/GTNElement.png

Fig. 26 Porosity and equivalent plastic strain evolution

./Figures/SimulationAndAnalysis/modelCompare/phaseFieldExample.png

(a) Distribution for d

./Figures/SimulationAndAnalysis/modelCompare/phaseFieldEpsPEq.png

(b) Equivalent plastic strain distribution

Fig. 27 Phase field fracture model

5.1.3 Phase field model

Property	Symbol	Value
Critical fracture energy	G_c	1×10^6 J/m^2
Plastic work threshold	W_o	0 J
Characteristic length	l	0.3266 mm

Table 13 Phase field fracture model parameters

The phase field fracture model predicts material degradation to be at its greatest towards the upper part of the wire. This is contrary to what we would expect. The phase-field fracture model does not distinguish between tensile and compressive stress states for the plastic contribution towards crack growth leading to this unrealistic behaviour. The region of greatest plastic straining corresponds to the region where material degradation is predicted to be highest.

5.2 Prediction of fracture

As well as the clear limitations in the GTN and phase field model described in the previous section, there are other factors which make them unsuitable for further investigation in the prediction of fracture in wire drawing processes. The phase field fracture model requires a relatively fine mesh [20] making it computationally expensive. The GTN model requires the calibration of multiple parameters, which is not feasible given the data available for the cases that will be looked at here. In order to rigorously calibrate these parameters, the characterization of each stage of ductile damage requires the continuous monitoring of void nucleation, growth and coalescence during deformation, which can be done using X-ray tomography measurements such as in Thuillier et al. [130] and Fansi et al. [131].

Lemaitre-based damage models with crack-closure effects are chosen for further evaluation. These models are set to incorporate crack-closure effects as in Teixeira [100], Pires [101], and described in section 4.2.7. The crack closure parameter h is assumed to be 0.2 here, as is typically the case for steels [86, 102, 103]. The Lemaitre exponent parameter b is generally assumed to be equal to 1.0 for ductile materials [72, 91]. A cut-off value for ξ of -0.33 below which damage does not accumulate is also assumed, given the experimental observations of Bao and Wierzbicki [98].

Both the classic Lemaitre [72] damage evolution equation and a novel Lemaitre-based formulation will be assessed. The damage evolution equation of the classic Lemaitre model is given by:

$$\dot{D} = \frac{\dot{\gamma}}{(1-D)} \left[\frac{-Y}{S_0} \right]^b \tag{69}$$

5.2.1 Proposed Law

As noted in Malcher et al. [91], the classic Lemaitre damage model has a tendency to predict fracture too early at low triaxialities and too late at high triaxialities values. To remedy this, a damage potential given in equation 7.3 has been proposed in Malcher and Mamiya [91].

$$F_D = \frac{S(\eta,\xi)}{(1-D)\,(b+1)} \left[\frac{-Y}{S(\eta,\xi)} \right]^{b+1} \tag{70}$$

Following the procedure described in section 4.2.3 of this thesis, the damage evolution equation is then given as

$$\dot{D} = \frac{\dot{\gamma}}{(1-D)} \left[\frac{-Y}{S(\eta,\xi)} \right]^b \tag{71}$$

The Lemaitre damage denominator is modified to become a function of the triaxiality η and in some cases the Lode parameter ξ. Various forms of the function $S(\eta, \xi)$ have been proposed to better predict fracture under a range of loading conditions [92, 93].

A function for $S(\eta, \xi)$ is proposed here (equation 72) which incorporates the triaxiality relationship used in the uncoupled damage law known as the Ko criterion [132]. The Ko criterion has shown an ability to predict fracture in both wire drawing processes [128] and in the hub-hole expanding process [132].

$$S(\eta) = \frac{2S_0}{(1.0 + 3\eta)} \tag{72}$$

For the wire drawing cases to be looked at in this chapter $\xi \approx 1.0$ at the centre of the wire (Appendix F.1) where fracture originates [128]. For this reason, the proposed function does not incorporate a dependency on ξ. The damage evolution law can be rewritten as:

$$\dot{D} = \frac{\dot{\gamma}}{1 - D} \left[\frac{-Y}{2S_0} (1.0 + 3\eta) \right]^b \tag{73}$$

In the following simulations, the damage is not set to 0.99 after exceeding the critical damage D_c (equation 4.47). This is because the crack path is not of interest given that the details of the fracture surface are not provided in Roh et al. [128]. In any case relatively small time steps are required to track the crack growth which is computationally expensive. As well as this, insight into the damage behaviour can be made by seeing how much the damage D exceeds D_c, in cases where it does. Furthermore, the non-local gradient equation is not incorporated into these simulations. As will be shown show later, the calibrated value for D_c is quite low meaning that localisation behaviour is limited. In any case, the mesh cell size is kept consistent in all simulations to ensure that any localisation behaviour that may occur is consistent between the simulations.

5.2.2 Tensile test and drawing data

In this chapter, experimental data obtained by Roh et al. [128] for high-carbon steel with chromium addition is used to investigate the ability of the Lemaitre-based damage models to accurately predict fracture in wire drawing. The data from this paper concerning wire drawing experiments for various die half-angles α and reduction ratios r of 20% and 36% is examined here. These drawing tests are conducted on a wire of initial diameter 13 mm. The case in Roh et al. [128] where $r = 36\%$ and $\alpha = 2°$ is not looked at in this work due to the fact Roh et al. attribute the fracture that occurs to the combination of high r and low α leading to excessive pulling force and friction effects that are not captured by the friction model used in the simulations. The improvement of the friction model to account for this is beyond the scope of this work.

A tensile test is also conducted by Roh et al. [128] for a round bar of diameter 6.25 mm and gauge length 12.5 mm until fracture (Figure 7.10). The dataset sampled from Roh et al. [128] which will be examined in this thesis is provided in Figure 7.10 and Table 7.9. In Figure 7.10 the engineering stress and strain until fracture are given for a tensile test. In Table 7.10, a set of wire drawing cases are given. Cases, where fracture was observed experimentally, are denoted by the symbol X.

./Figures/SimulationAndAnalysis/compareExperimentalSimulation/experimentalData.png

Fig. 28 Tensile test experimental data from [128]

Reduction (%)	Drawing half-angle (°)	Fracture
	2	O
	4	O
	6	O
20	8	O
	10	O
	12	X
	14	X
	16	X
	4	O
	6	O
	8	O
36	10	O
	12	X
	14	X
	16	X

Table 14 Results of drawing tests [128]

5.2.3 Calibration

The material parameters are calibrated using the tensile test data. The calibration procedure follows that of Masse [8], where the plastic hardening law is first calibrated against the experimental results up until the point where necking can begin to be observed ($\sim$ 6.5% engineering strain). By separating out the calibration of the plastic hardening law and the damage parameters, the calibration procedure is simplified and the risk of over-fitting is reduced. The Young's modulus, Poisson's ratio and initial yield stress are taken from Roh et al. [128]. These values are 200 GPa, 0.3 and 689 MPa respectively. The modified Voce Law (equation 74) [129] is chosen to describe the plastic hardening law as Cao [129] found that this law could well describe the hardening behaviour of high carbon steel in tensile, torsion and compression tests.

$$\sigma_y = \sigma_{yo} + (\sigma_{yinf} - \sigma_{yo} + k\bar{\varepsilon}^p)(1 - e^{-\beta\bar{\varepsilon}^p}) \tag{74}$$

5.2.4 Tensile test simulation

The tensile test is simulated using an axisymmetric mesh as shown in Figure 7.11, by making use of symmetries only a quarter of the specimen needs to be modelled. A cell size of 0.25 mm is used in the critical zone of the wire mesh where fracture is expected to occur.

./Figures/SimulationAndAnalysis/compareExperimentalSimulation/simTensileTest.png

Fig. 29 Tensile test mesh, marked cell in pink for where fracture initiates

Applied total displacement	u	1.3375 mm
Time step	Δt	0.01 s
Displacement increment	Δu	0.0125 mm

Table 15 loading conditions for case a

5.2.5 Plastic hardening parameters

A global-local approach is taken to the calibration of these parameters. First, 50 sample sets of values for σ_{yinf}, k and $beta$ are taken from the range of values given in Table 7.10 using Latin hypercube sampling [133].

Term	Range
σ_{yinf}	1.1-1.5 ($\times$10e3) MPa
k	0.05-0.5 ($\times$10e3) MPa
$beta$	25-80

Table 16 Parameter values to be sampled

A tensile test is simulated using each of these sets of values. The force-displacement curves that result from each of these simulations are then compared to the experimental data for up to 6.5% engineering strain (Figure 7.10) using the objective function in equation 75.

$$S(b_j) = \frac{1}{N}\sum_{i=1}^{N}\left(\frac{|F_i^{sim}(b_j) - F_{l,\ i}^{exp}|}{F_i^{exp}}\right) \tag{75}$$

where b_j is the vector of variables, N is the number of experimental points, F_i^{sim} is the value of the simulated force point and $F_{l,\ i}^{exp}$ is the experimental point determined by linear interpolation to a specified displacement. The results which minimise this objective function are then further optimised using the Nelder-Mead method [134] to refine the material parameters. The resulting parameters are given in Table 7.11

Term	Value
σ_{yinf}	1.34 ($\times 10e9$) MPa
k	0.104 ($\times 10e9$) MPa
$beta$	32.82

Table 17 Calibrated material parameters for the plastic hardening law

5.2.6 Lemaitre damage parameter

Secondly, the Lemaitre damage parameter S_0 is calibrated for each of the Lemaitre-based laws. To do this, 50 sample values for this are taken at constant intervals for the range given in Table 7.12. For each of the Lemaitre-based laws to be investigated, tensile test simulations are conducted for each of these values. The parameters that minimise the objective function (equation 76) are then further optimised using the Nelder-Mead method.

The objective function to be minimised is given in equation 76. For this objective function, simulated force values that are lower than the experimental values are punished. This is to ensure a solution is not obtained that performs well in the latter-middle part of the deformation path (engineering strain between 7% and 9%) but leads to an unrealistically high amount of necking ("1" in Figure 7.12). This in turn results in an unrealistically high level of plastic straining, triaxiality and ultimately damage in the critical region of the round bar. "2" in Figure 7.12 gives the simulated force-displacement curve for the parameter calibrated using the objective function in equation 76.

$$S(b_j) = \frac{1}{N}\sum_{i=1}^{N}\left(\frac{< F_i^{sim}(S_0) - F_{l,\ i}^{exp} > +6\times < -\left(F_i^{sim}(S_0) - F_{l,\ i}^{exp}\right) >}{F_i^{exp}}\right) \tag{76}$$

./Figures/SimulationAndAnalysis/compareExperimentalSimulation/compareNecking.png

Fig. 30 Comparison of simulated and experimental data

The critical damage parameter D_c can then be set as the max value for the simulated damage obtained at 10.7% engineering strain [106]. The resultant material parameters are given in Table 7.13.

Term	Range
$S0$	$5 - 25\ MPa$

Table 18 Parameter values to be sampled

Law	S_0	D_c
Classic Lemaitre	$13.81\ MPa$	0.078
Proposed Lemaitre	$14.29\ MPa$	0.087

Table 19 Calibrated material - classic Lemaitre damage law

The resultant force-displacement curves obtained using the calibrated parameters are given in Figure 7.13.

./Figures/SimulationAndAnalysis/compareExperimentalSimulation/compareAllLemaitreExp

Fig. 31 Comparison of simulated and experimental data

./Figures/SimulationAndAnalysis/compareExperimentalSimulation/compareSimDamage.png

(a) Damage vs. engineering strain

./Figures/SimulationAndAnalysis/compareExperimentalSimulation/compareSimEpsPeq.png

(b) Equivalent plastic strain vs. engineering strain

Fig. 32 Damage and equivalent plastic strain evolution at centre of specimen

./Figures/SimulationAndAnalysis/compareExperimentalSimu

./Figures/SimulationAndAnalysis/compareDamage

(a) Damage vs. engineering strain

(b) Equivalent plastic strain vs. engineering strain

Fig. 33 Damage and equivalent plastic strain evolution at centre of specimen

5.2.7 Geometry and loading conditions

Applied total displacement	u	30 mm
Time step	Δt	0.0005 s
Displacement increment	Δu	0.1 mm
Friction coefficient	μ	0.08

Table 20 Loading conditions for wire drawing case

Die inlet diameter	16 mm
Die outer diameter	20 mm
Die outlet diameter	11.627, 10.4 mm
Die semi-angles used	2, 4, 6, 8, 10, 12, 14, 16
Wire length	30 mm
Initial wire diameter	13 mm
Die cell size	0.25 mm
Wire cell size	0.25 mm

Table 21 Die and wire geometry

Wire length	l	50 mm
Applied total displacement	u	50 mm
Time step	Δt	0.00025 s
Displacement increment	Δu	0.05 mm

Table 22 Conditions for cases where $r = 36\%$, $\alpha = 4°$ and $r = 20\%$, $\alpha = 2°$

A 30 mm long wire was used for these simulations, aside from the cases where $r = 36\%$ and $\alpha = 4°$ and $r = 20\%$ and $\alpha = 2°$. In these cases, the loading conditions and wire geometry given in Table 7.16 are used.

A 0.25 mm mesh cell size was found to be sufficient to achieve a consistent solution for the drawing simulations (Appendix F2). Die outlet diameters of 11.627 mm and 10.4 mm are used which result in reductions of 20% and 36% respectively. The coefficient of friction is taken from Roh et al. [128]. Neither the specific geometry of the die nor the material properties of the die are specified in Roh et al. [128] so a conical die is assumed with material parameters as in Clancy [11]. The material properties for both die and wire are given in Tables 7.17 and 7.18. For each of these simulations, the damage is set to begin evolving after a displacement of 2 mm.

Term	Value
Young's modulus	200 GPa
Poisson's ration	0.3
Hardening law	$689 + (1340 - 689 + 104\bar{\varepsilon}^p)(1 - e^{-32.82\times\bar{\varepsilon}^p})$
S_0	13.81, 14.29
b	1.0
D_c	0.078, 0.087

Table 23 Wire material parameters

Term	Value
Young's modulus	600 GPa
Poisson's ration	0.22

Table 24 Die material parameters

5.3 Results and discussion

5.3.1 Damage evolution profile

An example of the damage distribution for the case where $r = 36\%$, $\alpha = 6°$, and the classic Lemaitre damage evolution equation is used, is given in Figure 7.15. For all of the cases looked at here, the damage is at a maximum towards the centre of the specimen. This is due to the fact that this is where the triaxiality, and relatedly, the positive stress tensor is highest (Figure 7.16). The relationship between the triaxiality η and the positive stress tensor τ^+ will be further explored later in this section.

The evolution of the equivalent plastic strain, triaxiality and damage for a given cell is provided in Figure 7.17. This cell is located at the centre of the wire and has a cell centre 1.66 mm to the right of the wire inlet at the initial time step. It can be observed that the damage evolution primarily occurs with the increase in triaxiality towards the latter stage of its plastic straining.

./Figures/SimulationAndAnalysis/compare36_12/36_6Damage.png

Fig. 34 Distribution of damage for $r = 36\%,\ \alpha = 6°$

./Figures/SimulationAndAnalysis/compare36_12/36_6tauPositive.png

(a) Positve stress tensor

./Figures/SimulationAndAnalysis/compare36_12/36_6Triaxi

(b) Triaxiality η

./Figures/SimulationAndAnalysis/compare36_12/36_6Dpxx.png

(c) Plastic strain increment - x-direction

Fig. 35 Distribution of fields for $r = 36\%,\ \alpha = 6°$

./Figures/SimulationAndAnalysis/compareCellData/cellCompare.png

Fig. 36 Evolution of variables

5.3.2 Comparison with experimental data

In Figure 7.18 the damage accumulated by the cell that is at the wire centre, and has exited the process zone (the region that is undergoing plastic straining) at the final time step is compared with the critical damage D_c and plotted for each case. It can be observed that both the classic and the novel formulations of the Lemaitre model are reasonably consistent with the experimental results. The classic model accurately predicts fracture for the 20% reduction cases however it overpredicts fracture in the 36% reduction cases. The novel Lemaitre-based model slightly underpredicts fracture in both the 20% and 36% reduction cases, with a value for D that is 90.4% and 90.8% of D_c respectively.

./Figures/SimulationAndAnalysis/compareExperimentalSimulation/20Reduction.p

(a) 20% Reduction

./Figures/SimulationAndAnalysis/compareExperimentalSimulation/36Reduction.p

(b) 36% Reduction

Fig. 37 Comparison of simulated and experimental fracture - shaded region for where fracture occurred in experiments

./Figures/SimulationAndAnalysis/compareCellData/compareWeightedTriaxAll.png

(a) Weighted triaxiality

./Figures/SimulationAndAnalysis/compareCellData/comparePlasticStrain.png

(b) Equivalent plastic strain

Fig. 38 Comparison of weighted triaxiality and equivalent plastic strain

In Figure 7.19 the resultant equivalent plastic strain and the weighted triaxiality η_w (equation 77) are given for each test case. These values are taken from the cases simulated using the novel formulation. The resultant values for these are extremely similar between the classic and novel formulations so only the values obtained for the novel formulation are displayed for clarity's sake.

$$\eta_w = \frac{1}{\bar{\varepsilon}^p} \int_0^{\bar{\varepsilon}^p} \eta \, d\bar{\varepsilon}^p \tag{77}$$

The differences in the accumulated damage value for each case and model can be explained by viewing this figure. The equivalent plastic strain is considerably higher in the 36% reduction cases than in the 20% reduction cases, while the triaxiality is greater, when $\alpha \geq 6°$, in the 20% reduction cases. The accumulated damage is largely determined by the level of plastic straining, and the triaxiality state as it undergoes this plastic straining. The added triaxiality dependence in the novel formulation leads to there being considerably lower accumulated damage in the low η_w cases compared to the classic formulation.

5.3.3 Scanning electron microscopy (SEM)

In Roh et al. [128], SEM analysis was conducted for many of the cases where fracture did not occur to observe the development of micro-voids around inclusions (non-metallic inclusions within the steel), and for the formation of micro-cracks. For an accurate damage model, there should be a correlation between the damage D and the observed level of micro-voids and micro-cracks.

In Figure 7.20, several micrographs are provided for a selection of the cases. The accumulated damage D normalised against the critical damage D_c for each of these cases is also provided in Table 7.19.

The normalised damage values for the novel model are reasonably consistent with the micrographs. Values of 0.23 and 0.34 are obtained for a) and b) in Figure 7.20 where micro-voids can be observed, while values of 0.58 and 0.57 are obtained for the cases where micro-cracking can be observed in d) and e). The normalised damage of 0.35 for case c) where a ruptured inclusion can be observed is very similar to the value obtained for case b) where only microvoids are observed. It can be seen in Figure 7.19 that the $\alpha = 4°$ case has a greater peak value for the triaxiality η, while in Figure 7.21 it is clear that the η_w is greater for the case where $\alpha = 8°$. The net effect of this is that the model calculated similar accrued damage for the two cases. Given that in case c) a ruptured inclusion can be observed, this would suggest that the triaxiality relationship for the novel model is marginally too aggressive.

For the classic Lemaitre damage model, the normalised damage values are somewhat consistent with the micrographs. As with Figure 7.18 however, there is evidence for overprediction of damage. As well as predicting a D/D_c value of 1.23 for case d) where fracture did not occur, values of 0.54 and 0.68 seem quite high for cases a) and b) where only micro-voids can be observed.

Conclusive remarks can be hard to make on the suitability of these damage models based on a small sample of micrographs, however. Ideally, SEM analysis would be conducted on tensile

./Figures/SimulationAndAnalysis/compareVoidGrowth/20_6.png

(a) $r = 20\%,\ \alpha = 6^\circ$

./Figures/SimulationAndAnalysis/compareVoidGrowth/36_4.

(b) $r = 36\%,\ \alpha = 4^\circ$

./Figures/SimulationAndAnalysis/compareVoidGrowth/36_8.png

(c) $r = 36\%,\ \alpha = 8^\circ$

./Figures/SimulationAndAnalysis/compareVoidGrowth/36_10

(d) $r = 36\%,\ \alpha = 10^\circ$

./Figures/SimulationAndAnalysis/compareVoidGrowth/20_10.png

(e) $r = 20\%,\ \alpha = 10^\circ$

Fig. 39 Scanning electron microscopy (SEM) micrographs for various combinations of the half-angle α and reduction ratios (images adapted from Roh et al. [128])

specimens that have undergone various engineering strains [135] to try better understand the expected pattern of void nucleation, growth and coalescence (micro-crack formation) for various D values.

Reduction (%)	Drawing half-angle (°)	Novel D/D_c	Classic D/D_c
20	6	0.23	0.54
	10	0.58	0.89
	4	0.34	0.68
36	8	0.35	0.93
	10	0.57	1.23

Table 25 D/D_c for selected drawing cases

./Figures/SimulationAndAnalysis/compareCellData/degreeCompare.png

Fig. 40 Comparison of triaxiality evolution in process zone

subsubsectionSimulated and experimental results discrepancy

There are various factors that could explain the differences between simulated and experimental results. One of these is experimental error, it can be observed in Figure 7.14 that there would be a sharp difference in the obtained D_c if there was only a small difference in the engineering strain to fracture. It's worth noting that in Roh et al. [128], the critical fracture value was selected at 10% engineering strain for the Ko fracture criterion. In this thesis, the critical damage value was selected at 10.7% engineering strain in order to be consistent with the experimental engineering stress-strain curve provided in Roh et al. [128].

Limitations in the proposed model could also explain the discrepancies. The added triaxiality relationship incorporated into the Lemaitre model was chosen as this is the relationship used in the Ko criterion [132] which has been validated in the prediction of both the hub-hole expanding process [132] and fracture in wire drawing [128]. However, perhaps a different relationship, whether that be in the linear relationship proposed or an exponential relationship, could have achieved more accurate results.

Another limitation could be the friction model used. In this chapter, a friction coefficient μ of 0.08 was assumed to be consistent with Roh et al. [128], however, a different friction model would alter the obtained results. In Figure 7.22 it can be observed how the accumulated damage changes with μ for the novel Lemaitre-based damage model.

Another important consideration, that to this author's eye has been neglected in the literature, is the strong association between the positive stress tensor τ^+ and the triaxiality η at low triaxiality values (< 0.33) that predominate in typical wire drawing cases. The normalised positive stress tensor τ^+_{norm} is defined here and given by equation 78 and is plotted against the triaxiality for selected cases in Figure 7.23. Further incorporation of the positive stress tensor into the damage evolution law, via τ^+_{norm}, may have the potential for a better description of material fracture

./Figures/SimulationAndAnalysis/compareExperimentalSimulation/frictionDamage.png

Fig. 41 Normalised damage vs. friction coeffiecient

behaviour. This could be incorporated into the existing Lemaitre-based laws by altering the function $S(\eta, \xi)$ to take the form given in equation 79. More experimental data, which include a range of experimental conditions where $\eta > 0.33$ is required to better distinguish between the effects of the positive stress tensor and the triaxiality.

$$\tau^+_{norm} = \frac{\tau^+ : \tau^+}{\tau : \tau} \tag{78}$$

$$S(\eta, \xi, \tau^+_{norm}) \tag{79}$$

./Figures/SimulationAndAnalysis/compareCellData/tauTriaxCompare.png

Fig. 42 Positive stress tensor vs. triaxiality

5.4 Rhie Chow Case setup

In order to explore the effect of the Rhie-Chow stabilisation term, various simulations are conducted for different values of the Rhie-Chow scale factor. The values of the Rhie-Chow scale factor used are $0.01, 0.02, 0.05, 0.1, 0.15$ and 0.2. The geometry of the cases are the same as in chapter 5. The cases looked at are as follows:

(a) Flat notched bar - non-local Lemaitre

Applied total displacement	u	0.6 mm
Time step	Δt	0.015 s
Displacement increment	Δu	0.017145 mm

Table 26 Loading conditions for case a

Property	Symbol	Value
Young's modulus	E	68.9 GPa
Poisson's ratio	v	0.33
Lemaitre damage denominator	S_0	0.5 MPa
Lemaitre damage exponent	b	1.0
Characteristic length	l_c	0.6325 mm
Hardening law	σ_y	$320 + 688 \times \bar{\varepsilon}^p$ MPa

Table 27 Material properties for case a

(b) Round notched bar - non-local Lemaitre

Applied total displacement	u	0.8 mm
Time step	Δt	0.015 s
Displacement increment	Δu	0.015 mm

Table 28 Loading conditions for case b

(c) Flat notched bar - phase field model

Property	Symbol	Value
Young's modulus	E	69.9 GPa
Poisson's ratio	v	0.3
Lemaitre damage denominator	S_0	1.1 MPa
Lemaitre damage exponent	b	1.0
Characteristic length	l_c	0.6325 mm
Hardening law	σ_y	$589(0.0001 + \bar{\varepsilon}^p)^{0.216}$ MPa

Table 29 Material properties for case b

Applied total displacement	u	0.41148 mm
Time step	Δt	0.015 s
Displacement increment	Δu	0.017145 mm

Table 30 loading conditions for case c

Property	Symbol	Value
Young's modulus	E	68.8 GPa
Poisson's ratio	v	0.33
Critical fracture energy	G_c	60×10^3 J/m^2
Plastic threshold	W_o	1×10^7 MPa
Characteristic length	l	0.3226mm
Hardening law	σ_y	$320 + 688 \times \bar{\varepsilon}^p$ MPa

Table 31 Material properties for case c

./Figures/RhieChowCompare/0.015_forceDispBordenNonLocalLemaitre.png

(a) Force vs. displacement

./Figures/RhieChowCompare/0.015_obj_BordenNonLocalLemai

(b) % difference vs. scale factor

Fig. 43 Case a - flat notched bar w) non-local Lemaitre

5.5 Results

For each of the cases, the following comparisons are made in the figures below

- The force-displacement curves are plotted together
- Through the use of an objective function (equation 6.3), the average percentage difference between the resultant force-displacement points for a Rhie-Chow scale factor of 0.01 are compared with those for Rhie-Chow scale factors $0.02, 0.05, 0.1, 0.15$ and 0.05

$$g_0(\boldsymbol{p}) = \frac{1}{N} \sum_{q=1}^{N} \left(\frac{R_q^{0.01}(\boldsymbol{p}) - R_q^{\mathcal{R}}}{R_q^{0.01}} \right) \tag{80}$$

It can be observed in the force-displacement curves (Figures 6.1a, 6.2a and 6.3a) that the Rhie-Chow term has the effect of slowing down the localisation behaviour of the models. In all cases, it

./Figures/RhieChowCompare/0.015_forceDispNonLocalLemaitreAxi.png

(a) Force vs. displacement

./Figures/RhieChowCompare/0.015_obj_nonLocalLemaitre...

(b) % difference vs. scale factor

Fig. 44 Case b - notched round bar w) non-local Lemaitre

./Figures/RhieChowCompare/0.015_forceDispPhaseBorden.png

(a) Force vs. displacement

./Figures/RhieChowCompare/0.015_obj_phaseBorden.png

(b) % difference vs. scale factor

Fig. 45 Case c - flat notched bar w) phase field fracture

can be seen that the rate at which the force declines with displacement is reduced with increasing Rhie-Chow scale factor.

5.5.1 Time step dependancy

The effects of the Rhie-Cow stabilisation term are reduced with smaller time steps. To illustrate the effect this has on damage and fracture behaviour, the cases described above are conducted with varying time steps, and therefore varying displacement increments.

Time step (Δt)	Displacement increment (Δu)
0.015	0.017145 mm
0.0125	0.0142875 mm
0.01	0.01143 mm
0.0075	0.0085725 mm
0.005	0.005715 mm
0.0025	0.0028575 mm

Table 32 Time steps with associated displacement increments for case a

In Figures 6.4, 6.5 and 6.6 the force-displacement curves for various Rhie-Chow scale factors and time step 0.001s are displayed. Comparing these with those obtained for a time step of 0.015s

Time step (Δt)	Displacement increment (Δu)
0.015	0.015 mm
0.0125	0.0125 mm
0.01	0.01 mm
0.0075	0.0075 mm
0.005	0.005 mm
0.0025	0.0025 mm

Table 33 Time steps with associated displacement increments for case b

Time step (Δt)	Displacement increment (Δu)
0.015	0.017145 mm
0.0125	0.0142875 mm
0.01	0.01143 mm
0.0075	0.0085725 mm
0.005	0.005715 mm
0.0025	0.0028575 mm

Table 34 Time steps with associated displacement increments for case c

(a) Force vs. displacement

(b) % difference vs. scale factor

Fig. 46 Case a - flat notched bar w) non-local Lemaitre

in the previous subsection, it is evident that the Rhie-Chow term is having less of an effect on the solution.

The reduction of the effects of the Rhie-Chow term with the time-step size is further quantified in Figure 6.7. In these figures, the objective function from equation 6.3 is used to quantify the difference between the force-displacements obtained with Rhie-Chow scale factors 0.01 and 0.1 for each time step given in Tables 6.7, 6.8 and 6.9.

It is evident that for case a and case b there is a reduction in the effects of the Rhie-Chow term with decreasing time step. This relationship is a little more complicated for case c. This is likely due to the fact that by varying the time steps, we are not just altering the Rhie-Chow effects, but given the time-step dependency inherent in the finite volume method, some aspects of the solution itself are being affected.

In order to illustrate the benefit of this proposed scheme, simulations are conducted for cases a, b and c with a time-step of 0.005 s. Rhie-Chow scaling fields of $\mathcal{R}_{field}(D) = (1-D)^2\ 0.1$ and $\mathcal{R}_{field}(d) = (1-d)^2\ 0.1$ are used for the Lemaitre and phase field model simulations respectively.

./Figures/RhieChowCompare/0.001_forceDispNonLocalLemaitreAxi.png

(a) Force vs. displacement

./Figures/RhieChowCompare/0.001_obj_nonLocalLemaitreA

(b) % difference vs. scale factor

Fig. 47 Case b - notched round bar w) non-local Lemaitre

./Figures/RhieChowCompare/0.001_forceDispPhaseBorden.png

(a) Force vs. displacement

./Figures/RhieChowCompare/0.001_obj_phaseBorden.png

(b) % difference vs. scale factor

Fig. 48 Case c - flat notched bar w) phase field fracture

The results from these simulations are compared with those obtained for Rhie-Chow scale factors of 0.1 and 0.01 in Figure 50.

It can be observed that the proposed strategy reduces the effect that the Rhie-Chow scale factor has on the localisation behaviour when employing the Rhie-Chow scale field $\mathcal{R}_{field}$ approach. The benefits to a higher Rhie-Chow scale factor (improved convergence properties, reduction of "checker-boarding errors") are therefore gained using this scheme up until the point where crack propagation begins to occur. At this point, the Rhie-Chow effects are reduced and therefore, its effect on the fracture behaviour is mitigated.

It is noticeable that the proposed strategy leads to lower reaction force for cases a and c (Figure 50). This is due to the fact that by reducing the scale factor below 0.01, these residual forces that exist after the crack propagation stage are reduced. These residual forces are somewhat non-physical in any case, as will be discussed in the next section.

5.6 Effective non-local test case

The benefits of this scheme can be seen in Figures 51 and 52. These figures show the results obtained with the novel formulation. For these simulations, the material parameter D_c is set as 0.55. A more

./Figures/RhieChowCompare/timeStep_BordenNonLocal.png

(a) % difference vs. time step - case a

./Figures/RhieChowCompare/timeStep_nonLocalLemaitreAxi.

(b) % difference vs. time step - case b

./Figures/RhieChowCompare/timeStep_phaseBorden.png

(c) % difference vs. time step - case c

Fig. 49 Comparison of Rhie-Chow effects with time-step size

physically realistic damage evolution can be observed as well as the rapid crack propagation being evident in the force-displacement curve. Such a rapid loss of load-carrying capacity at a certain point for tensile specimens has been observed experimentally [91, 136]. It is worth noting that the fact that the damage is set as 0.99 combined with the diffusive effects of the Rhie-Chow term will still lead to some nonphysical residual force-displacement behaviour of the simulations (e.g. the residual force required for further displacement in Figure 52).

5.7 Prediction of chevron cracks

This should be moved to the test cases

Applied total displacement	u	30 mm
Uncoupled displacement	u	50 mm
Time dtep	Δt	0.001 s
Displacement increment	Δu	2 mm
Friction coefficient	μ	0.1

Table 35 Loading conditions for wire drawing case

A common defect that occurs in wire drawing is the development of chevron cracks (or central burst defects) at the centre of the wire (Figure 53). The ability of the developed scheme is tested in its ability to model their occurrence. The relevant material properties and loading conditions

./Figures/finiteVolumeCharacteristics/0.005_forceDispBorden.png

(a) Case a

./Figures/finiteVolumeCharacteristics/0.005_forceDisp

(b) Case b

./Figures/finiteVolumeCharacteristics/0.005_forceDispPhase.png

(c) Case c

Fig. 50 Comparison of Rhie-Chow field approach with different Rhie-Chow scale factors

./Figures/effectiveNonLocalDamage/effNLDispForceBar.png

(a) Force vs. displacement

./Figures/effectiveNonLocalDamage/eff_disp_damageNonL

(b) non-local Damage vs. displacement

Fig. 51 Flat notched bar (case a)

are given in Tables 6.10-13 (further details on these wire drawing simulations are given in the next chapter).

./Figures/effectiveNonLocalDamage/effNLDispForceAxi.png

(a) Force vs. displacement

./Figures/effectiveNonLocalDamage/eff_disp_damageNonLoc

(b) non-local Damage vs. displacement

Fig. 52 Notched round bar (case b)

Die inlet diameter	16 mm
Die outlet diameter	11.6276 mm
Die outer diameter	20 mm
Die seim-angle	$10°$
Wire length	30 mm
Wire diameter	13 mm

Table 36 Die and wire geometry

Property	Symbol	Value
Young's modulus	E	200 GPa
Poisson's ratio	v	0.33
Lemaitre damage denominator	S_0	15 MPa
Lemaitre damage exponent	b	1.0
Critical Damage	D_c	0.052
Characteristic Length	l_c	0.325 mm
Hardening law	σ_y	$600 + (1218 - 600 + 250 \times \bar{\varepsilon}^p)(1 - e^{43.44 \times \bar{\varepsilon}^p})$ MPa

Table 37 Wire material properties

Property	Symbol	Value
Young's modulus	E	600000 GPa
Poisson's ratio	v	0.22

Table 38 Die material properties (linear elastic material law)

./Figures/finiteVolumeCharacteristics/chevronCracked.png

Fig. 53 Chevron cracks in steel rods, similar to those that can occur in drawn wires [137]

./Figures/finiteVolumeCharacteristics/simulatedChevron.png

(a) Axisymmetric mesh

./Figures/finiteVolumeCharacteristics/270ChevronCracking.png

(b) 270° rotational extrusion

Fig. 54 Chevron cracks in wire drawing

The accurate modelling of chevron cracks, using the developed effective non-local damage scheme, is evident in Figure 54. By contrast in Figure 55, the results can be seen if the growth of the local damage field D is not restricted when $\bar{D}_{eff} > D_c$ (step (i) in Algorithm **??**). The unrestricted growth of the local damage field D leads in turn to the rapid growth of the $\bar{D}$ field, and therefore a large number of cells have a value for $\bar{D}$ which exceeds D_c. The results of this are rapid crack propagation and an inability to predict the formation of chevron cracks (Figure 55 b).

./Figures/finiteVolumeCharacteristics/otherDrawing.png

(a) $\bar{D}_{eff}$ field prior to reaching D_c

./Figures/finiteVolumeCharacteristics/simulatedDrawingGrowth.png

(b) $\bar{D}_{eff}$ field after reaching D_c

Fig. 55 Unstable crack propogation

6 Conclusions

Short summary...

The following observations are made from the numerical analyses:

- main conclusions and take away points

Look toward future steps.

Acknowledgments. This work has emanated from research conducted with the financial support of/supported in part by a grant from Science Foundation Ireland (SFI) under Grant number RC2302_2 and SFI NexSys 21/SPP/3756. Financial support is gratefully acknowledged from the Irish Research Council through the Laureate program, grant number IRCLA/2017/45. Vikram Pakrashi would also like to acknowledge FlowDyn RDD/966 and SiSDATA EAPA_0040/2022. Additionally, the authors want to acknowledge project affiliates, Bekaert, through the Bekaert

University Technology Centre (UTC) at University College Dublin (www.ucd.ie/bekaert), and I-Form, funded by Science Foundation Ireland (SFI) Grant Number 16/RC/3872, co-funded under European Regional Development Fund and by I-Form industry partners.

Appendix A Appendix: Single Cell Verifications

In order to add a further point of comparison, the non-local Lemaitre damage model was also implemented in Abaqus/Standard - a commercial finite element-based software. This was implemented through a user subroutine (UMAT). The Abaqus software has an inbuilt GTN model that we can use to compare with as well.

In order to implement the diffusion equation for the non-local Lemaitre damage model, the approach laid out in Azinpour et al. [138] is employed in this work. In Azinpour et al. [138], the authors make use of the Abaqus' software ability to solve the steady-state heat conduction diffusion equation in coupled temperature-displacement problems.

$$q = -k\nabla^2 T \tag{A1}$$

where q is the source term, k is the material's conductivity and T is the temperature.

This equation is made compatible with the non-local gradient equation as shown in table 5.1.

Field	Field variable	Diffusion coefficient	Flux term	Source term
Temperature	T	k	$\nabla^2 T$	q
Non-local damage	$\bar{D}$	l_c^2	$\nabla^2 D$	$\bar{D} - D$

Table A1 Analogous set-up of the heat equation and non-local gradient equation

./figures/finiteVolumeImplementation/cubeCase.png

Fig. A1 one element case

In order to verify the implementation of these models, tests are conducted on an element of geometry 1 mm × 1 mm × 1 mm (Figure 5.1). The elements used in the solids4Foam toolbox have previously been validated through a patch test [139]. In this test case, a displacement is applied in the y direction to the top boundary of the element.

A.1 Lemaitre model

A displacement of 0.2 mm is applied with mechanical properties described in Table 5.2. These mechanical properties are taken from Autay et al. [140].

Property	Symbol	Value
Young's modulus	E	200 GPa
Poisson's ratio	v	0.3
Lemaitre damage denominator	S_0	0.5 MPa
Lemaitre damage exponent	b	1.0
Hardening law	σ_y	$200 + 10^3 \times \bar{\varepsilon}^p$ MPa

Table A2 Material properties for Lemaitre one cell test

The results gained from simulations in OpenFOAM and Abaqus are compared with the analytical relationships derived in Doghri [141] in Figure 5.2. The analytically derived relationship for the damage D as a function of the equivalent plastic strain $\bar{\varepsilon}^p$ is given by

$$(1-D)^2 = 1 - \frac{\sigma_{y0}^2}{3ES_0}\frac{\sigma_{y0}}{h}\left[\left(1+\frac{h}{\sigma_{y0}}\bar{\varepsilon}^p\right)^3 - 1\right]R_v \tag{A2}$$

where σ_{y0} and h are constants in the hardening law $\sigma_{y0} + h(\bar{\varepsilon}^p)$. R_v is given by:

$$R_v = \frac{2}{3}(1+v) + 3(1-2v)(\eta) \tag{A3}$$

where the triaxiality $\eta = 0.33$ for a uniaxial tensile test.

The analytical relationship for the equivalent stress σ_{eq} is also provided

$$\sigma_{eq} = (1-D)(\sigma_{y0} + h(\bar{\varepsilon}^p)) \tag{A4}$$

It can be observed that the damage increases in an exponential manner with respect to the equivalent plastic strain. This is due to the fact that with the material constant $b = 1$, the Damage increases with the square of the effective von Mises equivalent stress (equation 30).

The plastic strain in the Y direction ε^p_{yy} is also given as a function of the equivalent plastic strain $\bar{\varepsilon}^p$ and compared with the results obtained by Doghri [141] (Figure 5.3).

./figures/finiteVolumeImplementation/EpsPEQ_Damage.png

(a) Damage vs. equivalent plastic strain

./figures/finiteVolumeImplementation/EpsPEQ_EquivStress.png

(b) Equivalent stress vs. equivalent plastic strain

Fig. A2 Comparison between OpenFOAM, Abaqus and analytically derived relationships

./figures/finiteVolumeImplementation/plasticStrainMult.png

Fig. A3 Plastic strain (YY) vs. equivalent plastic strain

A.2 GTN model

Property	Symbol	Value
Young's modulus	E	200 GPa
Poisson's ratio	v	0.3
q1	$q1$	1.5
q2	$q2$	1
q3	$q3$	2.25
Initial porosity	f_0	0.002
Mean	ε_n	0.3
Standard deviation	S_n	0.1
Volume fraction	f_N	0.2
Hardening law	σ_y	$400 + 300 \times \bar{\varepsilon}^p$ MPa

Table A3 Material properties for GTN one cell test

In this section, the results for the GTN model implemented in OpenFOAM are compared with those obtained from the inbuilt GTN model in Abaqus. The material properties used are displayed in Table 5.3. The GTN model in Abaqus does not allow for the inclusion of porous failure criteria (equation 47) in Abaqus/Standard so this feature of the GTN model was neglected. The results are compared in Figure 5.4.

It is clear that there is strong agreement between Abaqus and the OpenFoam implementation. It is notable that the rate of porosity growth declines towards the latter stages of the deformation in Figure 5.4 a). This is due to the fact that the porosity growth due to the nucleation of voids is assumed to follow a Gaussian distribution (equation 50). As will be discussed in chapter **??**, this assumption is unlikely to be an accurate description of material behaviour.

./figures/GTNCompare/displacement_f.png

(a) Porosity vs. displacement

./figures/GTNCompare/displacement_sigmaEq.png

(b) Equivalent stress vs. displacement

./Figures/GTNCompare/EpsPEq_epsPY.png

(c) Plastic strain in the Y direction vs. Equivalent plastic strain

Fig. A4 Comparison between OpenFOAM and Abaqus

A.3 Phase field fracture

Property	Symbol	Value
Young's modulus	E	68.8 GPa
Poisson's ratio	v	0.33
Critical fracture energy	G_c	$138 \times 10^6\ J/m^2$
Plastic work threshold	w_0	$10^6\ J$
Characteristic length	l	2 m
Hardening law	σ_y	$320 + 688 \times \bar{\varepsilon}^p$ MPa

Table A4 Material properties for phase field fracture one cell test

Here the results obtained from a one-cell test are compared with those obtained by Borden et al. [20] in Figure 5.5.

In this test case, the cell undergoes a rapid loss of load-carrying capacity (Figure 5.6). This is due to the fact that after the plastic work threshold is exceeded, there is a rapid increase in the plastic strain energy contribution to the crack-driving force $\mathcal{H}$ and therefore growth of the phase field variable d. The combination of this and the fact that the crack degradation function is proportional to the square of the phase field ($g_e(d) = (1-d)^2$) leads to the swift reduction in the equivalent stress.

./Figures/finiteVolumeImplementation/phaseField/displacement_EpsPYY.png

(a) Plastic strain vs. total strain

./Figures/finiteVolumeImplementation/phaseField/displacement_sigmaEq.png

(b) Equivalent stress vs. total strain

Fig. A5 Comparison between OpenFOAM and [20]

./figures/finiteVolumeImplementation/phaseField/displacement_degredationFucntion.png

(a) Crack degradation function g(d) vs. total strain

./figures/finiteVolumeImplementation/phaseField/displacement_phaseField.png

(b) Phase field (d) vs. total strain

Fig. A6 Evolution of d and the crack degradation Function

Appendix B Phase Field Model Updated-to-Total Lagrangian Transformation

Given that the mesh is moved to the updated configuration after each time step, the non-local equation is solved with respect to this updated mesh configuration. However, sometimes it may be preferred to solve the non-local equation with respect to the initial mesh configuration.

It's worth noting however that the results from the non-local equation will differ if the non-local gradient equation is solved with respect to the initial configuration Ω_o. If the non-local equation is solved with respect to the updated configuration, then in tension the non-local damage will tend towards the local damage as the distance between the cell centres will increase. Conversely, in compressive states, the distances between cell centres will decrease leading to greater diffusion in the region of a damaged cell. In order to illustrate this, simulations on a one-dimensional bar of length $10mm$ were performed. An imperfection is placed at the centre of the bar so that here the local damage $D = 1.0$. In all other cells $D = 0$. Both 20% compressive and tensile strains were applied. It can be seen in Figure B7 how the distribution of the non-local damage is therefore altered as the bar undergoes tension and compression

./Figures/damageModels/compressiveTensileDamage.png

Fig. B7 Non-local damage along the original bar length

It remains a matter of debate in the literature as to whether solving this equation with respect to the initial or updated configuration is preferable [97]. Steinmann [142] has argued that the fact that the non-local damage will tend towards the local damage (in an object undergoing tensile loading) is an argument for solving with respect to the initial configuration to ensure that the mesh independence of the solution remains strong. However, he also noted that this may not be physically realistic as it is not likely the case that a material's non-local properties are completely independent of its deformation path.

In order to ensure that solving the non-local gradient equation with respect to the initial configuration is possible, within the context of an updated Lagrangian solid model, a mathematical and algorithmic approach was developed in this work. This approach allows for the solving of the non-local gradient equation with respect to the initial configuration within the context of an updated Lagrangian solid model framework.

To begin, the strong integral form of the non-local equation with respect to the initial configuration is stated:

$$\int_{\Omega_o} D \; d\Omega_o - \int_{\Omega_o} \bar{D} \; d\Omega_o + \oint_{\Gamma_o} {l_c}^2 \; \mathbf{n}_o \cdot \nabla \bar{\mathrm{D}} \; d\Gamma_o = 0 \tag{B5}$$

Given the definition of the volume change J, the volume in the updated configuration can be related to the initial volume:

$$J_n^{-1} V_u = V_o \tag{B6}$$

where J_n is the volume change from the previous time step. Nanson's formula is employed to describe the updated Γ_u area vector in terms of the initial area vector Γ_o:

$$\mathbf{\Gamma_u} = J_n \mathbf{F}_n^{-T} \cdot \mathbf{\Gamma}_0 \tag{B7}$$

The initial area vector Γ_o can then be rewritten in terms of the updated area vector Γ_u:

$$J_n^{-1} \mathbf{F}_n^T \cdot \mathbf{\Gamma_u} = \mathbf{\Gamma}_0 \tag{B8}$$

Using equation B6, the first two volume integral terms in equation B8 can be given in terms of the updated configuration as:

$$\int_{\Omega_o} D \; d\Omega_o = \int_{\Omega_u} J_n^{-1} D \; d\Omega_u \tag{B9}$$

$$\int_{\Omega_o} \bar{D} \; d\Omega_o = \int_{\Omega_u} J_n^{-1} \bar{D} \; d\Omega_u \tag{B10}$$

Gauss' theorem can then be used to reformulate the gradient term within the third term of equation B5:

$$\oint_{\Gamma_o} {l_c}^2 \; \mathbf{n}_o \cdot \nabla \bar{\mathrm{D}} \; d\Gamma_o = \oint_{\Gamma_o} {l_c}^2 \; \mathbf{n}_o \cdot \left(\oint_{\Gamma_o} \mathbf{n}_o \bar{D} \; d\Gamma_o \right) \; d\Gamma_o \tag{B11}$$

The term on the right-hand side of equation B11 can then be reformulated in terms of the updated configuration by combining it with equation B8 to give

The full equation to be solved is therefore

Algorithmic approach

Equation **??** is solved as shown in equation B12, with the second and third terms added in to aid with convergence. The divergence, gradient and Laplacian terms are discretised using the Gauss linear scheme [59]. A user-defined number of outer iterations are performed around this equation. The code for its implementation is provided in Appendix C.

$$
\begin{aligned}
\underbrace{\int_{\Omega_u} J_n^{-1} \bar{D}\, d\Omega_u}_{\text{implicit}} - & \underbrace{\oint_{\Gamma_u} \mathbf{n}_u \cdot \nabla \left(\Delta \bar{\mathrm{D}}\right) d\Gamma_u}_{\text{implicit}} \\
& + \underbrace{\oint_{\Gamma_u} \mathbf{n}_u \cdot \nabla \left(\Delta \bar{\mathrm{D}}\right) d\Gamma_u}_{\text{explicit}} \\
& - \underbrace{\oint_{\Gamma_u} {l_c}^2 \left(J_n^{-1} \mathbf{F}_n^T \cdot \mathbf{n}_u\right) \cdot \left(\oint_{\Gamma_u} \left(J_n^{-1} \mathbf{F}_n^T \cdot \mathbf{n}_u\right) \bar{D}\, d\Gamma_u\right) d\Gamma_u}_{\text{explicit}} \\
& = \underbrace{\int_{\Omega_u} J_n^{-1} \bar{D}\, d\Omega_u}_{\text{explicit}}
\end{aligned}
\tag{B12}
$$

B.1 Validation of updated-Lagrangian to reference approach

In this section, the implementation of the approach described in section **??** is verified. This is done by simulating each of case a and case b (from section 5.4) in the following three ways

- With an updated Lagrangian solid model
- With a total Lagrangian solid model
- with an updated Lagrangian solid model and the non-local damage gradient equation solved with respect to the initial configuration

The force-displacement curves for these simulations are given in Figure B8. The results of the UL to reference approach and the total Lagrangian approach line up well. However, in Figure 6.17 a, a slight discrepancy can be observed which given that very fine time-steps and meshes are used for these simulations is unrelated to discritisation error (Appendix A.1). Is unclear why this exists. It may be due to slight differences in the discretisation techniques - in the UL to reference approach the divergence of the gradient of the non-local damage variable $\bar{D}$ is solved for, whereas in the total Lagrangian approach the option in OpenFOAM to solve the Laplacian directly is used. Some differences in the Rhie-Chow effects between the total-Lagrangian and updated-Lagrangian approach may also contribute.

./Figures/finiteVolumeCharacteristics/bordenLagCompare_ForceDisp.png

(a) Flat notched bar - case a

./Figures/finiteVolumeCharacteristics/axiLagCompare_ForceDisp.png

(b) Notched round bar - case b

Fig. B8 Comparison of approaches

References

[1] Riccio, A. (ed.): Damage Growth in Aerospace Composites, 1st ed. 2015 edn. Springer Aerospace Technology. Springer, Cham (2015). https://doi.org/10.1007/978-3-319-04004-2

[2] Johnson, A.F., Toso-Pentecôte, N., Schueler, D.: Numerical modelling of impact and

damage tolerance in aerospace composite structures. In: Numerical Modelling of Failure in Advanced Composite Materials, pp. 479–506. Elsevier, ??? (2015). https://doi.org/10.1016/B978-0-08-100332-9.00018-9 . https://linkinghub.elsevier.com/retrieve/pii/B9780081003329000189 Accessed 2022-12-06

[3] Alharbi, K., Ghadbeigi, H., Efthymiadis, P., Zanganeh, M., Celotto, S., Dashwood, R., Pinna, C.: Damage in dual phase steel DP1000 investigated using digital image correlation and microstructure simulation. Modelling and Simulation in Materials Science and Engineering **23**(8), 085005 (2015) https://doi.org/10.1088/0965-0393/23/8/085005 . Accessed 2022-12-06

[4] Sirinakorn, T., Uthaisangsuk, V., Srimanosawapal, S.: Microstructure based Description of Deformation Behavior of Dual Phase Steel Sheets. Procedia Engineering **81**, 1366–1371 (2014) https://doi.org/10.1016/j.proeng.2014.10.158 . Accessed 2022-12-06

[5] Sarraf, I.S.: Meso–Scale Modelling of Deformation, Damage and Failure in Dual Phase Steels. PhD thesis, University of Windsor (2017)

[6] Uthaisangsuk, V., Prahl, U., Bleck, W.: Characterisation of formability behaviour of multiphase steels by micromechanical modelling. International Journal of Fracture **157**(1-2), 55–69 (2009) https://doi.org/10.1007/s10704-009-9329-4 . Accessed 2022-12-06

[7] Chen, Y.: Modeling of Ductile Fracture Using Local Approach : Reliable Simulation of Crack Extension. PhD thesis, École des Mines de Paris (2020)

[8] Masse, T.: Study and Optimization of High Carbon Steel Flat Wires. PhD thesis, École des Mines de Paris (2010)

[9] Cao, T.S.: Models for ductile damage and fracture prediction in cold bulk metal forming processes: a review. International Journal of Material Forming **10**(2), 139–171 (2017) https://doi.org/10.1007/s12289-015-1262-7 . Accessed 2022-12-06

[10] Tekkaya, A.E., Bouchard, P.-O., Bruschi, S., Tasan, C.C.: Damage in metal forming. CIRP Annals **69**(2), 600–623 (2020) https://doi.org/10.1016/j.cirp.2020.05.005 . Accessed 2022-12-06

[11] Clancy, M.: Improving the predictive capabilities of wire processing simulations. PhD thesis, University College Dublin (2019)

[12] Borchers, C., Kirchheim, R.: Cold-drawn pearlitic steel wires. Progress in Materials Science **82**, 405–444 (2016) https://doi.org/10.1016/j.pmatsci.2016.06.001 . Accessed 2023-01-06

[13] Cardiff, P., Tuković, v., Jaeger, P.D., Clancy, M., Ivanković, A.: A Lagrangian cell-centred finite volume method for metal forming simulation. International Journal for Numerical Methods in Engineering **109**(13), 1777–1803 (2017) https://doi.org/10.1002/nme.5345 . Accessed 2022-10-27

[14] Besson, J.: Continuum Models of Ductile Fracture: A Review. International Journal of Damage Mechanics **19**(1), 3–52 (2010) https://doi.org/10.1177/1056789509103482 . Accessed 2022-01-13

[15] Sumpter, J.: An Experimental Investigation of the. In: Hackett, E., Schwalbe, K.-H., Dodds, R. (eds.) Constraint Effects in Fracture, pp. 492–49211. ASTM International, 100 Barr Harbor Drive, PO Box C700, West Conshohocken, PA 19428-2959 (1993). https://doi.org/10.1520/STP18042S . http://www.astm.org/doiLink.cgi?STP18042S Accessed 2022-01-13

[16] O'Dowd, N.P., Shih, C.F.: Family of crack-tip fields characterized by a triaxiality parameter—I. Structure of fields. Journal of the Mechanics and Physics of Solids **39**(8), 989–1015 (1991) https://doi.org/10.1016/0022-5096(91)90049-T . Accessed 2022-01-13

[17] James, M.A., Newman, J.C.: The effect of crack tunneling on crack growth: experiments and CTOA analyses. Engineering Fracture Mechanics **70**(3-4), 457–468 (2003) https://doi.org/10.1016/S0013-7944(02)00131-5 . Accessed 2022-01-13

[18] Mahmoud, S., Lease, K.: The effect of specimen thickness on the experimental characterization of critical crack-tip-opening angle in 2024-T351 aluminum alloy. Engineering Fracture Mechanics **70**(3-4), 443–456 (2003) https://doi.org/10.1016/S0013-7944(02)00130-3 . Accessed 2022-01-13

[19] Ambati, M., Gerasimov, T., De Lorenzis, L.: Phase-field modeling of ductile fracture. Computational Mechanics **55**(5), 1017–1040 (2015) https://doi.org/10.1007/s00466-015-1151-4 . Accessed 2022-01-13

[20] Borden, M.J., Hughes, T.J.R., Landis, C.M., Anvari, A., Lee, I.J.: A phase-field formulation for fracture in ductile materials: Finite deformation balance law derivation, plastic degradation, and stress triaxiality effects. Computer Methods in Applied Mechanics and Engineering **312**, 130–166 (2016) https://doi.org/10.1016/j.cma.2016.09.005 . Accessed 2022-01-13

[21] Miehe, C., Aldakheel, F., Raina, A.: Phase field modeling of ductile fracture at finite strains: A variational gradient-extended plasticity-damage theory. International Journal of Plasticity **84**, 1–32 (2016) https://doi.org/10.1016/j.ijplas.2016.04.011 . Accessed 2022-01-13

[22] Dittmann, M., Aldakheel, F., Schulte, J., Wriggers, P., Hesch, C.: Variational phase-field formulation of non-linear ductile fracture. Computer Methods in Applied Mechanics and Engineering **342**, 71–94 (2018) https://doi.org/10.1016/j.cma.2018.07.029 . Accessed 2022-12-08

[23] Samaniego, C., Ulloa, J., Rodríguez, P., Houzeaux, G., Vázquez, M., Samaniego, E.: A phase-field model for ductile fracture with shear bands: A parallel implementation. International Journal of Mechanical Sciences **200**, 106424 (2021) https://doi.org/10.1016/j.ijmecsci.2021.106424 . Accessed 2022-12-08

[24] Martins, M.M., Bressan, J.D., Button, S.T., Ivankovic, A., Chinesta, F., Chastel, Y., El Mansori, M.: Extrusion Process by Finite Volume Method Using OpenFoam Software, Paris, (France), pp. 1461–1466 (2011). https://doi.org/10.1063/1.3552393 . http://aip.scitation.org/doi/abs/10.1063/1.3552393 Accessed 2022-10-27

[25] Basic, H., Demirdžić, I., Muzaferija, S.: Finite volume method for simulation of extrusion processes. International Journal for Numerical Methods in Engineering **62**(4), 475–494 (2005)

https://doi.org/10.1002/nme.1168 . Accessed 2022-12-08

[26] Maire, P.-H., Breil, J., Galera, S.: A cell-centred arbitrary Lagrangian–Eulerian (ALE) method. International Journal for Numerical Methods in Fluids **56**(8), 1161–1166 (2008) https://doi.org/10.1002/fld.1557 . Accessed 2023-08-06

[27] Cardiff, P., Demirdžić, I.: Thirty Years of the Finite Volume Method for Solid Mechanics. Archives of Computational Methods in Engineering **28**(5), 3721–3780 (2021) https://doi.org/10.1007/s11831-020-09523-0 . Accessed 2022-10-27

[28] Demirdžić, I., Martinović, D.: Finite volume method for thermo-elasto-plastic stress analysis. Computer Methods in Applied Mechanics and Engineering **109**(3-4), 331–349 (1993) https://doi.org/10.1016/0045-7825(93)90085-C . Accessed 2022-10-27

[29] Cardiff, P., Tuković, v., Jasak, H., Ivanković, A.: A block-coupled Finite Volume methodology for linear elasticity and unstructured meshes. Computers & Structures **175**, 100–122 (2016) https://doi.org/10.1016/j.compstruc.2016.07.004 . Accessed 2022-12-08

[30] Leonard, M., Murphy, N., Karač, A., Ivanković, A.: A numerical investigation of spherical void growth in an elastic–plastic continuum. Computational Materials Science **64**, 38–40 (2012) https://doi.org/10.1016/j.commatsci.2012.04.015 . Accessed 2022-12-08

[31] Bressan, J.D., Martins, M.M., Button, S.T.: Analysis of Aluminium Hot Extrusion by Finite Volume Method. Materials Today: Proceedings **2**(10), 4740–4747 (2015) https://doi.org/10.1016/j.matpr.2015.10.007 . Accessed 2022-12-08

[32] Maneeratana, K.: Development of the Finite Volume Method for Non-Linear Structural Applications. PhD, Imperial College, London (2000)

[33] Cardiff, P., Karač, A., Ivanković, A.: Development of a finite volume contact solver based on the penalty method. Computational Materials Science **64**, 283–284 (2012) https://doi.org/10.1016/j.commatsci.2012.03.011 . Accessed 2022-10-27

[34] Cardiff, P., Karač, A., FitzPatrick, D., Flavin, R., Ivanković, A.: Development of a Hip Joint Model for Finite Volume Simulations. Journal of Biomechanical Engineering **136**(1), 011006 (2014) https://doi.org/10.1115/1.4025776 . Accessed 2022-12-08

[35] Safari, A., Tukovic, Z., Cardiff, P., Walter, M., Casey, E., Ivankovic, A.: Interfacial separation of a mature biofilm from a glass surface – A combined experimental and cohesive zone modelling approach. Journal of the Mechanical Behavior of Biomedical Materials **54**, 205–218 (2016) https://doi.org/10.1016/j.jmbbm.2015.09.013 . Accessed 2023-01-26

[36] Carolan, D., Tuković, v., Murphy, N., Ivanković, A.: Arbitrary crack propagation in multi-phase materials using the finite volume method. Computational Materials Science **69**, 153–159 (2013) https://doi.org/10.1016/j.commatsci.2012.11.049 . Accessed 2023-01-30

[37] Ivankovic, A., Demirdžić, I., Williams, J.G., Leevers, P.S.: Application of the finite volume method to the analysis of dynamic fracture problems. International Journal of Fracture **66**(4), 357–371 (1994) https://doi.org/10.1007/BF00018439 . Accessed 2023-08-14

[38] Martínez-Ferrer, P.J., Qian, L., Ma, Z., Causon, D.M., Mingham, C.G.: An efficient finite-volume method to study the interaction of two-phase fluid flows with elastic structures. Journal of Fluids and Structures **83**, 54–71 (2018) https://doi.org/10.1016/j.jfluidstructs.2018.08.019 . Accessed 2022-10-27

[39] Greenshields, C.J., Weller, H.G.: A unified formulation for continuum mechanics applied to fluid-structure interaction in flexible tubes. International Journal for Numerical Methods in Engineering **64**(12), 1575–1593 (2005) https://doi.org/10.1002/nme.1409 . Accessed 2022-12-08

[40] Giannopapa, C.G., Papadakis, G.: Linear Stability Analysis and Application of a New Solution Method of the Elastodynamic Equations Suitable for a Unified Fluid-Structure-Interaction Approach. Journal of Pressure Vessel Technology **130**(3), 031303 (2008) https://doi.org/10.1115/1.2937764 . Accessed 2022-12-08

[41] Greenshields, C.J., Venizelos, G.P., Ivankovic, A.: A FLUID–STRUCTURE MODEL FOR FAST BRITTLE FRACTURE IN PLASTIC PIPES. Journal of Fluids and Structures **14**(2), 221–234 (2000) https://doi.org/10.1006/jfls.1999.0258 . Accessed 2022-12-08

[42] Schäfer, M., Teschauer, I.: Numerical simulation of coupled fluid–solid problems. Computer Methods in Applied Mechanics and Engineering **190**(28), 3645–3667 (2001) https://doi.org/10.1016/S0045-7825(00)00290-5 . Accessed 2022-12-08

[43] Belytschko, T., Liu, W.K., Moran, B., Elkhodary, K.I.: Nonlinear Finite Elements for Continua and Structures, Second edition edn. Wiley, Chichester, West Sussex, United Kingdon (2014)

[44] Hassan, O.I., Ghavamian, A., Lee, C.H., Gil, A.J., Bonet, J., Auricchio, F.: An upwind vertex centred finite volume algorithm for nearly and truly incompressible explicit fast solid dynamic applications: Total and Updated Lagrangian formulations. Journal of Computational Physics: X **3**, 100025 (2019) https://doi.org/10.1016/j.jcpx.2019.100025 . Accessed 2023-01-26

[45] Vaz, M., Muñoz-Rojas, P.A., Filippini, G.: On the accuracy of nodal stress computation in plane elasticity using finite volumes and finite elements. Computers & Structures **87**(17-18), 1044–1057 (2009) https://doi.org/10.1016/j.compstruc.2009.05.007 . Accessed 2023-09-02

[46] Demirdžić, I., Martinović, D., Ivankovic, A.: Numerical simulation of thermal deformation in welded workpiece (1988). https://www.researchgate.net/publication/296148474_Numerical_simulation_of_thermal_deformation_in_welded_workpiece

[47] Demirdžić, I., Muzaferija, S.: Finite volume method for stress analysis in complex domains. International Journal for Numerical Methods in Engineering **37**(21), 3751–3766 (1994) https://doi.org/10.1002/nme.1620372110 . Accessed 2023-01-26

[48] Trangenstein, J.A., Colella, P.: A higher-order Godunov method for modeling finite deformation in elastic-plastic solids. Communications on Pure and Applied Mathematics **44**(1), 41–100 (1991) https://doi.org/10.1002/cpa.3160440103 . Accessed 2023-01-26

[49] Sevilla, R., Giacomini, M., Huerta, A.: A face-centred finite volume method for second-order

elliptic problems: A face-centred finite volume method for second-order elliptic problems. International Journal for Numerical Methods in Engineering **115**(8), 986–1014 (2018) https://doi.org/10.1002/nme.5833 . Accessed 2023-01-26

[50] Sevilla, R., Giacomini, M., Huerta, A.: A locking-free face-centred finite volume (FCFV) method for linear elasticity (2018) https://doi.org/10.48550/ARXIV.1806.07500 . Publisher: arXiv Version Number: 1. Accessed 2023-02-01

[51] Lee, C.H., Gil, A.J., Bonet, J.: Development of a cell centred upwind finite volume algorithm for a new conservation law formulation in structural dynamics. Computers & Structures **118**, 13–38 (2013) https://doi.org/10.1016/j.compstruc.2012.12.008 . Accessed 2023-01-26

[52] Haider, J., Lee, C.H., Gil, A.J., Bonet, J.: A first-order hyperbolic framework for large strain computational solid dynamics: An upwind cell centred Total Lagrangian scheme: A CELL CENTRED FINITE VOLUME METHOD FOR LARGE STRAIN SOLID DYNAMICS. International Journal for Numerical Methods in Engineering **109**(3), 407–456 (2017) https://doi.org/10.1002/nme.5293 . Accessed 2023-02-01

[53] Haider, J., Lee, C.H., Gil, A.J., Huerta, A., Bonet, J.: An upwind cell centred Total Lagrangian finite volume algorithm for nearly incompressible explicit fast solid dynamic applications. Computer Methods in Applied Mechanics and Engineering **340**, 684–727 (2018) https://doi.org/10.1016/j.cma.2018.06.010 . Accessed 2023-01-26

[54] Maire, P.-H., Nkonga, B.: Multi-scale Godunov-type method for cell-centered discrete Lagrangian hydrodynamics. Journal of Computational Physics **228**(3), 799–821 (2009) https://doi.org/10.1016/j.jcp.2008.10.012 . Accessed 2023-08-27

[55] Cardiff, P., Tang, T., Tukovic, Z., Jasak, H., Ivankovic, A., De Jaeger, P.: An Eulerian-inspired Lagrangian finite volume method for wire drawing simulations, National University of Ireland, Galway, Ireland (2017)

[56] Bathe, K.-J.: Finite Element Procedures. Prentice Hall, Englewood Cliffs, N.J (1996)

[57] Jasak, H., Weller, H.G.: Application of the finite volume method and unstructured meshes to linear elasticity. International Journal for Numerical Methods in Engineering **48**(2), 267–287 (2000) https://doi.org/10.1002/(SICI)1097-0207(20000520)48:2⟨267::AID-NME884⟩3.0.CO;2-Q . Accessed 2022-02-08

[58] Cardiff, P., Karač, A., Ivanković, A.: A large strain finite volume method for orthotropic bodies with general material orientations. Computer Methods in Applied Mechanics and Engineering **268**, 318–335 (2014) https://doi.org/10.1016/j.cma.2013.09.008 . Accessed 2022-12-09

[59] OpenFOAM Programmer's Guide (2015)

[60] Batistić, I., Cardiff, P., Tuković: A finite volume penalty based segment-to-segment method for frictional contact problems. Applied Mathematical Modelling **101**, 673–693 (2022) https://doi.org/10.1016/j.apm.2021.09.009

[61] Batistić, I., Cardiff, P., Ivanković, A., Tuković, v.: A finite volume penalty-based implicit procedure for the treatment of the frictionless contact boundaries. International Journal for Numerical Methods in Engineering **124**(18), 4171–4191 (2023)

[62] Rhie, C.M., Chow, W.L.: Numerical study of the turbulent flow past an airfoil with trailing edge separation. AIAA Journal **21**(11), 1525–1532 (1983) https://doi.org/10.2514/3.8284 . Accessed 2022-12-01

[63] Demirdžić, I., Muzaferija, S.: Numerical method for coupled fluid flow, heat transfer and stress analysis using unstructured moving meshes with cells of arbitrary topology. Computer Methods in Applied Mechanics and Engineering **125**(1-4), 235–255 (1995) https://doi.org/10.1016/0045-7825(95)00800-G . Accessed 2022-02-03

[64] Bijelonja, I.: Finite volume method for incremental analysis of small and large thermo-elasto-plastic deformations. PhD thesis, University of Sarajevo (2002). In Bosnian

[65] Bijelonja, I., Demirdžić, I., Muzaferija, S.: A finite volume method for large strain analysis of incompressible hyperelastic materials. International Journal for Numerical Methods in Engineering **64**, 1594–1609 (2005)

[66] Bijelonja, I.: FINITE VOLUME METHOD ANALYSIS OF LARGE STRAIN ELASTO-PLASTIC DEFORMATION. In: The 16^{th} DAAAM International Symposium, Opatia, Croatia (2005)

[67] Bijelonja, I., Demirdžić, I., Muzaferija, S.: A finite volume method for incompressible linear elasticity. Computer Methods in Applied Mechanics and Engineering **195**, 6378–6390 (2006)

[68] Jacobs, D.A.H.: A Generalization of the Conjugate-Gradient Method to Solve Complex Systems. IMA Journal of Numerical Analysis **6**(4), 447–452 (1986) https://doi.org/10.1093/imanum/6.4.447 . Accessed 2022-10-28

[69] Karypis, G., Kumar, V.: A fast and highly quality multilevel scheme for partitioning irregular graphs. SIAM Journal on Scientific Computing **20**(1), 359–392 (1999)

[70] Pellegrini, F.: Scotch and PT-Scotch Graph Partitioning Software: An Overview. In: Uwe Naumann, O.S. (ed.) Combinatorial Scientific Computing, pp. 373–406. Chapman and Hall/CRC, ??? (2012). https://doi.org/10.1201/b11644-15 . https://inria.hal.science/hal-00770422

[71] Garrison, W.M., Moody, N.R.: Ductile fracture. Journal of Physics and Chemistry of Solids **48**(11), 1035–1074 (1987) https://doi.org/10.1016/0022-3697(87)90118-1 . Accessed 2023-01-05

[72] Lemaitre, J.: A Continuous Damage Mechanics Model for Ductile Fracture. Journal of Engineering Materials and Technology **107**(1), 83–89 (1985) https://doi.org/10.1115/1.3225775 . Accessed 2022-01-13

[73] Lemaître, J., Desmorat, R.: Engineering Damage Mechanics: Ductile, Creep, Fatigue and Brittle Failures. Springer, Berlin ; New York (2005). OCLC: ocm56646827

[74] Gurson, A.L.: Continuum Theory of Ductile Rupture by Void Nucleation and Growth: Part I—Yield Criteria and Flow Rules for Porous Ductile Media. Journal of Engineering Materials and Technology **99**(1), 2–15 (1977) https://doi.org/10.1115/1.3443401 . Accessed 2022-01-13

[75] Tvergaard, V., Needleman, A.: Analysis of the cup-cone fracture in a round tensile bar. Acta Metallurgica **32**(1), 157–169 (1984) https://doi.org/10.1016/0001-6160(84)90213-X . Accessed 2022-01-13

[76] Bai, Y., Wierzbicki, T.: A new model of metal plasticity and fracture with pressure and Lode dependence. International Journal of Plasticity **24**(6), 1071–1096 (2008) https://doi.org/10.1016/j.ijplas.2007.09.004 . Accessed 2022-03-11

[77] Nahshon, K., Hutchinson, J.W.: Modification of the Gurson Model for shear failure. European Journal of Mechanics - A/Solids **27**(1), 1–17 (2008) https://doi.org/10.1016/j.euromechsol.2007.08.002 . Accessed 2022-03-11

[78] Eterovic, A.L., Bathe, K.-J.: A hyperelastic-based large strain elasto-plastic constitutive formulation with combined isotropic-kinematic hardening using the logarithmic stress and strain measures. International Journal for Numerical Methods in Engineering **30**(6), 1099–1114 (1990) https://doi.org/10.1002/nme.1620300602 . Accessed 2023-01-05

[79] Koji, M., Bathe, K.-J.: Inelastic Analysis of Solids and Structures. Springer, Berlin; [London (2010). OCLC: 781682619

[80] Souza Neto, E.A., Peri, D., Owen, D.R.J.: Computational Methods for Plasticity. John Wiley & Sons, Ltd, Chichester, UK (2008). https://doi.org/10.1002/9780470694626 . http://doi.wiley.com/10.1002/9780470694626 Accessed 2022-01-13

[81] Simo, J.C., Hughes, T.J.R.: Computational Inelasticity. Interdisciplinary applied mathematics, vol. v. 7. Springer, New York (1998)

[82] Papadopoulos, P., Lu, J.: On the formulation and numerical solution of problems in anisotropic finite plasticity. Computer Methods in Applied Mechanics and Engineering **190**(37-38), 4889–4910 (2001) https://doi.org/10.1016/S0045-7825(00)00355-8 . Accessed 2023-01-05

[83] Mettler, L.K.: Numerical Implementation of an Anisotropic Finite-Deformation Plasticity Model (2012) https://doi.org/10.3929/ETHZ-A-009774144 . Medium: application/pdf,Online-Ressource Publisher: ETH Zurich. Accessed 2022-01-13

[84] Caminero, M.A., Montáns, F.J., Bathe, K.-J.: Modeling large strain anisotropic elasto-plasticity with logarithmic strain and stress measures. Computers & Structures **89**(11-12), 826–843 (2011) https://doi.org/10.1016/j.compstruc.2011.02.011 . Accessed 2022-11-23

[85] Andrade, F.X.C., Sá, J.M.A., Andrade Pires, F.M.: A Ductile Damage Nonlocal Model of Integral-type at Finite Strains: Formulation and Numerical Issues. International Journal of Damage Mechanics **20**(4), 515–557 (2011) https://doi.org/10.1177/1056789510386850 . Accessed 2022-03-16

[86] Bouchard, P.-O., Bourgeon, L., Fayolle, S., Mocellin, K.: An enhanced Lemaitre model formulation for materials processing damage computation. International Journal of Material Forming **4**(3), 299–315 (2011) https://doi.org/10.1007/s12289-010-0996-5 . Accessed 2022-12-11

[87] Cao, T.-S., Gachet, J.-M., Montmitonnet, P., Bouchard, P.-O.: A Lode-dependent enhanced Lemaitre model for ductile fracture prediction at low stress triaxiality. Engineering Fracture Mechanics **124-125**, 80–96 (2014) https://doi.org/10.1016/j.engfracmech.2014.03.021 . Accessed 2022-01-13

[88] Chandrakanth, S., Pandey, P.C.: An isotropic damage model for ductile material. Engineering Fracture Mechanics **50**(4), 457–465 (1995) https://doi.org/10.1016/0013-7944(94)00214-3 . Accessed 2023-01-06

[89] Wei Hua Tai, Bing Xian Yang: A new microvoid-damage model for ductile fracture. Engineering Fracture Mechanics **25**(3), 377–384 (1986) https://doi.org/10.1016/0013-7944(86)90133-5 . Accessed 2023-01-06

[90] Bonora, N.: A nonlinear CDM model for ductile failure. Engineering Fracture Mechanics **58**(1-2), 11–28 (1997) https://doi.org/10.1016/S0013-7944(97)00074-X . Accessed 2023-01-06

[91] Malcher, L., Mamiya, E.N.: An improved damage evolution law based on continuum damage mechanics and its dependence on both stress triaxiality and the third invariant. International Journal of Plasticity **56**, 232–261 (2014) https://doi.org/10.1016/j.ijplas.2014.01.002 . Accessed 2022-12-10

[92] Ferreira, G., Campos, E., Neves, R., Desmorat, R., Malcher, L.: An improved continuous damage model to estimate multiaxial fatigue life under strain control problems. International Journal of Damage Mechanics **31**(6), 815–844 (2022) https://doi.org/10.1177/10567895221091306 . Accessed 2022-12-15

[93] Castro, F., Bemfica, C.: Calibration and evaluation of the Lemaitre damage model using axial- torsion fatigue tests on five engineering alloys. Latin American Journal of Solids and Structures **15**(10) (2018) https://doi.org/10.1590/1679-78254340 . Accessed 2022-12-15

[94] Lian, J., Feng, Y., Münstermann, S.: A Modified Lemaitre Damage Model Phenomenologically Accounting for the Lode Angle Effect on Ductile Fracture. Procedia Materials Science **3**, 1841–1847 (2014) https://doi.org/10.1016/j.mspro.2014.06.297 . Accessed 2022-10-06

[95] Peerlings, R.H.J., Geers, M.G.D., Borst, R., Brekelmans, W.A.M.: A critical comparison of nonlocal and gradient-enhanced softening continua. International Journal of Solids and Structures **38**(44-45), 7723–7746 (2001) https://doi.org/10.1016/S0020-7683(01)00087-7 . Accessed 2022-12-05

[96] Peerlings, R.H.J., de Borst, R., Brekelmans, W.A.M., Geers, M.G.D.: Localisation issues in local and nonlocal continuum approaches to fracture. European Journal of Mechanics - A/Solids **21**(2), 175–189 (2002) https://doi.org/10.1016/S0997-7538(02)01211-1 . Accessed 2022-01-13

[97] Geers, M.G.D., Ubachs, R.L.J.M., Engelen, R.A.B.: Strongly non-local gradient-enhanced finite strain elastoplasticity. International Journal for Numerical Methods in Engineering **56**(14), 2039–2068 (2003) https://doi.org/10.1002/nme.654 . Accessed 2022-01-13

[98] Bao, Y., Wierzbicki, T.: On the cut-off value of negative triaxiality for fracture. Engineering Fracture Mechanics **72**(7), 1049–1069 (2005) https://doi.org/10.1016/j.engfracmech.2004.07.011 . Accessed 2022-10-11

[99] Chu, C.C., Needleman, A.: Void Nucleation Effects in Biaxially Stretched Sheets. Journal of Engineering Materials and Technology **102**(3), 249–256 (1980) https://doi.org/10.1115/1.3224807 . Accessed 2022-01-13

[100] Teixeira, P.M.C.: Ductile Damage Prediction in Sheet Metal Forming and Experimental Validation. PhD thesis, Faculdade de Engenharia da Universidade do Porto (2010)

[101] Pires, F.M.A.: Issues on the Finite Element Modelling of Degradation and Prediction of Failure in Finitely Straining Ductile Materials. PhD thesis, University of Wales Swansea (2005)

[102] Desmorat, R., Cantournet, S.: Modeling Microdefects Closure Effect with Isotropic/Anisotropic Damage. International Journal of Damage Mechanics **17**(1), 65–96 (2008) https://doi.org/10.1177/1056789507069541 . Accessed 2022-12-11

[103] Lemaitre, J.: A Course on Damage Mechanics, 2., rev. and enlarged ed edn. Springer, Berlin (1996)

[104] Bettaieb, M.B., Lemoine, X., Duchêne, L., Habraken, A.M.: On the numerical integration of an advanced Gurson model. International Journal for Numerical Methods in Engineering **85**(8), 1049–1072 (2011) https://doi.org/10.1002/nme.3010 . Accessed 2023-01-06

[105] Achouri, M., Germain, G., Dal Santo, P., Saidane, D.: Numerical integration of an advanced Gurson model for shear loading: Application to the blanking process. Computational Materials Science **72**, 62–67 (2013) https://doi.org/10.1016/j.commatsci.2013.01.035 . Accessed 2023-01-06

[106] Malcher, L.: Continuum Modelling and Numerical Simulation of Damage for Ductile Materials. PhD, University of Porto (2012)

[107] Leclerc, J., Nguyen, V.-D., Pardoen, T., Noels, L.: A micromechanics-based non-local damage to crack transition framework for porous elastoplastic solids. International Journal of Plasticity **127**, 102631 (2020) https://doi.org/10.1016/j.ijplas.2019.11.010 . Accessed 2023-01-06

[108] Reusch, F., Svendsen, B., Klingbeil, D.: A non-local extension of Gurson-based ductile damage modeling. Computational Materials Science **26**, 219–229 (2003) https://doi.org/10.1016/S0927-0256(02)00402-0 . Accessed 2023-01-06

[109] Borden, M.J., Verhoosel, C.V., Scott, M.A., Hughes, T.J.R., Landis, C.M.: A phase-field description of dynamic brittle fracture. Computer Methods in Applied Mechanics and

Engineering **217-220**, 77–95 (2012) https://doi.org/10.1016/j.cma.2012.01.008 . Accessed 2022-01-13

[110] Miehe, C., Hofacker, M., Welschinger, F.: A phase field model for rate-independent crack propagation: Robust algorithmic implementation based on operator splits. Computer Methods in Applied Mechanics and Engineering **199**(45-48), 2765–2778 (2010) https://doi.org/10.1016/j.cma.2010.04.011 . Accessed 2022-01-13

[111] Francfort, G.A., Marigo, J.-J.: Revisiting brittle fracture as an energy minimization problem. Journal of the Mechanics and Physics of Solids **46**(8), 1319–1342 (1998) https://doi.org/10.1016/S0022-5096(98)00034-9 . Accessed 2022-03-16

[112] Mumford, D., Shah, J.: Optimal approximations by piecewise smooth functions and associated variational problems. Communications on Pure and Applied Mathematics **42**(5), 577–685 (1989) https://doi.org/10.1002/cpa.3160420503 . Accessed 2022-03-16

[113] Ambrosio, L., Tortorelli, V.M.: Approximation of functional depending on jumps by elliptic functional via t-convergence. Communications on Pure and Applied Mathematics **43**(8), 999–1036 (1990) https://doi.org/10.1002/cpa.3160430805 . Accessed 2022-03-16

[114] Bourdin, B., Larsen, C.J., Richardson, C.L.: A time-discrete model for dynamic fracture based on crack regularization. International Journal of Fracture **168**(2), 133–143 (2011) https://doi.org/10.1007/s10704-010-9562-x . Accessed 2023-01-03

[115] Amor, H., Marigo, J.-J., Maurini, C.: Regularized formulation of the variational brittle fracture with unilateral contact: Numerical experiments. Journal of the Mechanics and Physics of Solids **57**(8), 1209–1229 (2009) https://doi.org/10.1016/j.jmps.2009.04.011 . Accessed 2022-03-22

[116] Miehe, C., Hofacker, M., Welschinger, F.: A phase field model for rate-independent crack propagation: Robust algorithmic implementation based on operator splits. Computer Methods in Applied Mechanics and Engineering **199**(45-48), 2765–2778 (2010) https://doi.org/10.1016/j.cma.2010.04.011 . Accessed 2022-01-13

[117] Eldahshan, H., Munoz, D.P., Alves, J., Perchat, E., Bouchard, P.-O.: 3D crack initiation and propagation applied to metal forming processes. International Journal of Material Forming **15**(5), 60 (2022) https://doi.org/10.1007/s12289-022-01702-7 . Accessed 2023-01-06

[118] Sá, J.M.A., Areias, P.M.A., Zheng, C.: Damage modelling in metal forming problems using an implicit non-local gradient model. Computer Methods in Applied Mechanics and Engineering **195**(48-49), 6646–6660 (2006) https://doi.org/10.1016/j.cma.2005.02.037 . Accessed 2022-01-13

[119] Fincato, R., Tsutsumi, S.: A return mapping algorithm for elastoplastic and ductile damage constitutive equations using the subloading surface method. International Journal for Numerical Methods in Engineering **113**(11), 1729–1754 (2018) https://doi.org/10.1002/nme.5718 . Accessed 2022-11-23

[120] Vaz, M., Owen, D.R.J.: Aspects of ductile fracture and adaptive mesh refinement in damaged elasto-plastic materials. International Journal for Numerical Methods in Engineering **50**(1), 29–54 (2001) https://doi.org/10.1002/1097-0207(20010110)50:1⟨29::AID-NME18⟩3.0.CO;2-G . Accessed 2022-11-23

[121] Eldahshan, H., Bouchard, P.-O., Alves, J., Perchat, E., Munoz, D.P.: Phase field modeling of ductile fracture at large plastic strains using adaptive isotropic remeshing. Computational Mechanics **67**(3), 763–783 (2021) https://doi.org/10.1007/s00466-020-01962-7 . Accessed 2022-03-22

[122] Soyarslan, C., Tekkaya, A.E.: Finite deformation plasticity coupled with isotropic damage: Formulation in principal axes and applications. Finite Elements in Analysis and Design **46**(8), 668–683 (2010) https://doi.org/10.1016/j.finel.2010.03.006 . Accessed 2023-03-14

[123] Cardiff, P., Tang, T., Tukovic, Z., Jasak, H., Ivankovic, A., De Jaeger, P.: An Eulerian-inspired Lagrangian finite volume method for wire drawing simulations, National University of Ireland, Galway, Ireland (2017)

[124] González, A.A., Celentano, D.J., Cruchaga, M.A.: Assessment of ductile failure models in single-pass wire drawing processes. International Journal of Damage Mechanics **27**(9), 1291–1306 (2018) https://doi.org/10.1177/1056789517704029 . Accessed 2022-12-13

[125] Norasethasopon, S., Yoshida, K.: Prediction of chevron crack initiation in inclusion copper shaped-wire drawing. Engineering Failure Analysis **15**(4), 378–393 (2008) https://doi.org/10.1016/j.engfailanal.2007.01.003 . Accessed 2023-01-01

[126] Zimerman, Z., Darlington, H., Kottcamp, E.H.: Selection of Operating Parameters to Prevent Central Bursting Defects During Cold Extrusion. In: Hoffmanner, A.L. (ed.) Metal Forming: Interrelation Between Theory And Practice, pp. 47–62. Springer, Boston, MA (1971). https://doi.org/10.1007/978-1-4615-1757-3_2 . http://link.springer.com/10.1007/978-1-4615-1757-3_2 Accessed 2023-01-01

[127] Choi, J.-S., Lee, H.-C., Im, Y.-T.: A study on chevron crack formation and evolution in a cold extrusion. Journal of Mechanical Science and Technology **24**(9), 1885–1890 (2010) https://doi.org/10.1007/s12206-010-0605-z . Accessed 2023-01-01

[128] Roh, Y.-H., Cho, D., Choi, H.-C., Yang, Z., Lee, Y.: Process Condition Diagram Predicting Onset of Microdefects and Fracture in Cold Bar Drawing. Metals **11**(3), 479 (2021) https://doi.org/10.3390/met11030479 . Accessed 2022-12-10

[129] Cao, T.-S.: Modelling Ductile Damage for Complex Loading Paths. PhD, École des Mines de Paris (2014)

[130] Thuillier, S., Maire, E., Brunet, M.: Ductile damage in aluminium alloy thin sheets: Correlation between micro-tomography observations and mechanical modeling. Materials Science and Engineering: A **558**, 217–225 (2012) https://doi.org/10.1016/j.msea.2012.07.116 . Accessed 2022-12-10

[131] Fansi, J., Balan, T., Lemoine, X., Maire, E., Landron, C., Bouaziz, O., Ben Bettaieb, M.,

Marie Habraken, A.: Numerical investigation and experimental validation of physically based advanced GTN model for DP steels. Materials Science and Engineering: A **569**, 1–12 (2013) https://doi.org/10.1016/j.msea.2013.01.019 . Accessed 2022-12-10

[132] Ko, Y.K., Lee, J.S., Huh, H., Kim, H.K., Park, S.H.: Prediction of fracture in hub-hole expanding process using a new ductile fracture criterion. Journal of Materials Processing Technology **187-188**, 358–362 (2007) https://doi.org/10.1016/j.jmatprotec.2006.11.071 . Accessed 2022-12-11

[133] Loh, W.-L.: On Latin hypercube sampling. The Annals of Statistics **24**(5) (1996) https://doi.org/10.1214/aos/1069362310 . Accessed 2022-12-11

[134] Luersen, M.A., Le Riche, R.: Globalized Nelder–Mead method for engineering optimization. Computers & Structures **82**(23-26), 2251–2260 (2004) https://doi.org/10.1016/j.compstruc.2004.03.072 . Accessed 2022-12-11

[135] Liu, X., Liu, Y., Jin, B., Lu, Y., Lu, J.: Microstructure Evolution and Mechanical Properties of a SMATed Mg Alloy under In Situ SEM Tensile Testing. Journal of Materials Science & Technology **33**(3), 224–230 (2017) https://doi.org/10.1016/j.jmst.2016.11.012 . Accessed 2022-12-20

[136] Li, H., Fu, M.W., Lu, J., Yang, H.: Ductile fracture: Experiments and computations. International Journal of Plasticity **27**(2), 147–180 (2011) https://doi.org/10.1016/j.ijplas.2010.04.001 . Accessed 2022-12-02

[137] Krauss, G.: Steels: Processing, Structure, and Performance, Second edition edn. ASM International, Materials Park, Ohio (2015). OCLC: ocn904652440

[138] Azinpour, E., Ferreira, J.P.S., Parente, M.P.L., Sa, J.C.: A simple and unified implementation of phase field and gradient damage models. Advanced Modeling and Simulation in Engineering Sciences **5**(1), 15 (2018) https://doi.org/10.1186/s40323-018-0106-7 . Accessed 2022-11-09

[139] Cardiff, P.: Patch Test. https://solids4foam.github.io/tutorials/more-tutorials/solid-mechanics/linearElasticity/patchTest.html

[140] Autay, R., Koubaa, S., Wali, M., Dammak, F.: Numerical Implementation of Coupled Anisotropic Plasticity-Ductile Damage in Sheet Metal Forming Process. Journal of Mechanics **34**(4), 417–430 (2018) https://doi.org/10.1017/jmech.2017.28 . Accessed 2022-11-14

[141] Doghri, I.: Numerical implementation and analysis of a class of metal plasticity models coupled with ductile damage. International Journal for Numerical Methods in Engineering **38**(20), 3403–3431 (1995) https://doi.org/10.1002/nme.1620382004 . Accessed 2022-01-13

[142] Steinmann, P.: Formulation and computation of geometrically non-linear gradient damage. International Journal for Numerical Methods in Engineering, 757–779